Commun. Comput. Phys.
doi: 10.4208/cicp.190315.290316a

Vol. **20**, No. 3, pp. 619-659
September 2016

Practical Techniques in Ghost Fluid Method for Compressible Multi-Medium Flows

Liang Xu[1], Chengliang Feng[2] and Tiegang Liu[2,*]

[1] *China Academy of Aerospace Aerodynamics, Beijing 100074, P.R. China.*
[2] *LMIB and School of Mathematics and Systems Science, Beijing University of Aeronautics and Astronautics, Beijing 100191, P.R. China.*

Communicated by Boo-Cheong Khoo

Received 19 March 2015; Accepted (in revised version) 29 March 2016

Abstract. The modified ghost fluid method (MGFM), due to its reasonable treatment for ghost fluid state, has been shown to be robust and efficient when applied to compressible multi-medium flows. Other feasible definitions of the ghost fluid state, however, have yet to be systematically presented. By analyzing all possible wave structures and relations for a multi-medium Riemann problem, we derive all the conditions to define the ghost fluid state. Under these conditions, the solution in the real fluid region can be obtained exactly, regardless of the wave pattern in the ghost fluid region. According to the analysis herein, a practical ghost fluid method (PGFM) is proposed to simulate compressible multi-medium flows. In contrast with the MGFM where three degrees of freedom at the interface are required to define the ghost fluid state, only one degree of freedom is required in this treatment. However, when these methods proved correct in theory are used in computations for the multi-medium Riemann problem, numerical errors at the material interface may be inevitable. We show that these errors are mainly induced by the single-medium numerical scheme in essence, rather than the ghost fluid method itself. Equipped with some density-correction techniques, the PGFM is found to be able to suppress these unphysical solutions dramatically.

AMS subject classifications: 35L45, 65C20, 76T10

Key words: Modified ghost fluid method, ghost fluid state, multi-medium Riemann problem, general equation of state, compressible multi-medium flow.

1 Introduction

The dynamics of compressible multi-medium flows often give rise to challenging problems in both theory and numerical simulation. The change in equation of state (EOS) is

*Corresponding author. *Email addresses:* xul@buaa.edu.cn (L. Xu), fengchengliang@163.com (C. Feng), liutg@buaa.edu.cn (T. Liu)

 ©2016 Global-Science Press

https://doi.org/10.4208/cicp.190315.290316a Published online by Cambridge University Press

known to cause numerical inaccuracies or oscillations near material interfaces. In order to overcome this difficulty, various strategies have been pursued in the past two decades with an even increasing interest [1–9]. Some methods treat materials that are separated by distinct sharp interfaces by reformulating the problem using a mixture model [1–6]. An artificial EOS is usually introduced for mixture cells. This treatment, however, may fail to capture discontinuous response and result in numerical instabilities, if a shock is transmitted across an interface for instance. Comparatively speaking, an immiscible model seems to be more reasonable in the presence of sharp interfaces. Researchers can take all kinds of effective measures such as volume of fluid method [10] or more popular level set technique [11] or front tracking technique [12] to deal with it. But the interfacial state, especially when nonlinear wave interaction occurring at the interface, should be faithfully simulated to suppress any undesired numerical oscillations.

The idea of ghost fluid method (GFM), originally suggested and developed by Glimm et al. [13, 14], has provided us a simple and flexible way for handling multi-medium flows with immiscible material interfaces. The GFM-based techniques [15–19] have been improved upon and applied by many researchers to a range of problems. By specially defining the ghost fluid state, the computation can be carried out as if in a single medium. The numerical schemes for single-medium flow can be employed without any changes and the methods are easily extended to multi-dimensions. These variants in GFMs differ in the way in which the ghost fluid state is populated.

Fedkiw et al. proposed the original GFM (OGFM) [15] by using the local real fluid velocity and pressure to define the corresponding ghost fluid state. Later, the gas-water version GFM (GWGFM) [16], where the ghost fluid state is defined by employing the velocity from the water and the pressure from the gas, was specially presented for coupling non-stiff fluid (gas) and stiff fluid (water). Although the two GFMs are problem-related and not suitable for some cases like high speed jet impacting [20], the simplicity and the easy extension to multi-dimensions promote the development of these methods [6, 21–23]. In order to take into account the effects of wave interaction and material properties, Liu et al. proposed the modified GFM (MGFM) [17] by carrying out characteristic analysis on the waves arriving at the interface and solving the local Riemann problem. Following the idea of Riemann-problem-based technique, the interface-interaction GFM (IGFM) [18] and the real GFM (RGFM) [19] have also been developed recently. The Riemann-problem-based algorithm, discussed in this paper, is characterized by (approximately) solving a multi-medium Riemann problem to define the ghost fluid state. This differs from the OGFM and the GWGFM where the ghost fluid states are defined via using the local flow state or extrapolating from the real fluid. These Riemann-problem-based techniques have been shown to be robust and less problem-related and successfully applied to solve a multitude of problems involving strong shocks interacting with gas-gas, gas-water interfaces and even fluid-structure coupling problems [17–20, 24–28]. Furthermore, it has been proved that the error estimate by the MGFM is "third-order accurate" in the vicinity of the interface for a multi-medium Riemann problem [29, 30].

Besides the MGFM where the ghost fluid state is defined by using the interfacial state,

https://doi.org/10.4208/cicp.190315.290316a Published online by Cambridge University Press

other feasible definitions of the ghost fluid state have yet to be systematically presented. One objective of this work, therefore, is to systematically analyze all possible ways of exactly defining the ghost fluid state for the multi-medium Riemann problem with a general EOS. We shall establish all relationships between interfacial state and ghost fluid state under the assumption of different wave structures in the ghost fluid region. If one type of these relationships is satisfied when defining the ghost fluid state for a multi-medium Riemann problem, the exact result in the real fluid region can definitely be obtained in theory, regardless of the wave pattern in the ghost fluid region.

However, these ways to define the ghost fluid state are highly relevant to wave structures in the ghost fluid region and sometimes too complicated to be performed in practice. Therefore, another aim of the present work is to discuss various practical methods to simulate multi-medium flows. A simple and effective Riemann-problem-based technique to define the ghost fluid state is presented. This technique is called practical GFM (PGFM) for ease of discussion in this work. We shall show that the PGFM, as the MGFM, has the interface error and the local conservation error of both "third-order accuracy" regardless of the solution type. More importantly, compared with the MGFM where all the interfacial pressure, velocity and density are required in the definition of the ghost fluid state, only the interfacial velocity is required using the PGFM. This implies that there is only one degree of freedom contributing to selecting the ghost fluid states in the PGFM. It may be noted that the "degree of freedom" discussed in this work should be understood or interpreted as the number of independent interfacial quantities which can be used to define the ghost fluid state. With the help of interfacial quantities in defining the ghost fluid state, the flow state on the other side should be exactly consistent with the state of the original multi-medium Riemann problem. It should not be explained as the number of independent quantities which must be defined in the ghost region for computational purposes, as mentioned in [15, 31].

Especially, unfavorable errors of underpredicting the density are usually localized close to the interface in some cases. According to several numerical experiments, we shall further show that such unphysical phenomenon is essentially induced by single-medium numerical schemes, rather than the treatments presented in this work for a multi-medium Riemann problem. Some density-correction techniques are designed to mitigate the material interface errors. Comparison of the results from different methods shows that the PGFM with the density-correction technique is able to suppress error generation and produce satisfactory results.

The paper is organized as follows. In Section 2 we introduce the Euler equations with multi-medium Riemann problem and a general form of EOS. Section 3 is devoted to some preliminary work for the following analysis. In this section, the solution structure of multi-medium Riemann problem and the general MGFM-based algorithm are presented. The objective of Section 4 is to identify all possible wave patterns in the ghost fluid region and to obtain the relationship between the exact interfacial state and the ghost fluid state. Also in this section, an air-water Riemann problem is taken as an example to validate the theoretical analysis. On the basis of the methodology obtained, the detailed imple-

https://doi.org/10.4208/cicp.190315.290316a Published online by Cambridge University Press

mentation of PGFM is presented in Section 5. Some basic properties of the PGFM are also shown in this section. The reason of error generation and the technique of error suppression are discussed in Section 6. In Section 7, the performance of PGFM in numerical simulations is shown and compared with the MGFM. Finally, conclusions are drawn in Section 8.

2 Equations

2.1 Governing equations and Riemann problem

The governing equations for one-dimensional inviscid and compressible flow are Euler equations, which can be written for an initial-value Riemann problem as follows:

$$\frac{\partial U}{\partial t}+\frac{\partial F(U)}{\partial x}=0,\quad U|_{t=0}=\begin{cases} U_L, & x<x_0,\\ U_R, & x>x_0,\end{cases} \tag{2.1}$$

where U and $F(U)$ are the vectors of conserved variables and fluxes, given respectively by $U=[\rho,\rho u,E]^T$, $F(U)=[\rho u,\rho u^2+p,(E+p)u]^T$. Here ρ is the density, u is the velocity, p is the pressure, and E is the total energy per unit volume. The total energy is written as

$$E=\rho e+\frac{1}{2}\rho u^2, \tag{2.2}$$

where e is the internal energy per unit mass. U_L and U_R are two constant states separated by the material interface located at x_0. Hereafter, the subscripts "L" and "R" indicate the flow state on the left- and right-hand medium, respectively. Once the diaphragm separating U_L and U_R is removed, the interface recovers to its normal motion instantly, where the initial pressure and velocity discontinuities disappear simultaneously.

2.2 Equation of state (EOS)

For closure of system (2.1), an EOS is required. A system in thermodynamic equilibrium can be completely described by some basic thermodynamic variables, such as pressure p, density ρ, internal energy e, entropy s, and temperature T. From thermodynamics it is known that only two of these parameters are independent. It is advantageous to chose p and ρ as the two independent variables. The EOS is then the equation that relates e to p and ρ:

$$e=e(p,\rho). \tag{2.3}$$

Many different media have a (2.3) type EOS. For example, the EOS for compressible gas and water can be expressed in a consistent form of

$$e=\frac{p+\gamma B}{(\gamma-1)\rho}. \tag{2.4}$$

https://doi.org/10.4208/cicp.190315.290316a Published online by Cambridge University Press

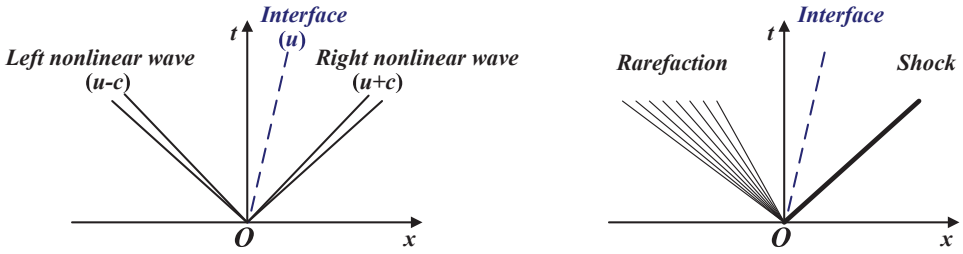
Here γ and B are set to γ_g and 0 for gas, to γ_w and B_w for water accordingly. More concretely, γ_g is the ratio of specific heats for gas. It is set to 1.4 for air. γ_w and B_w are set to 7.15 and 3.309×10^8 Pa, respectively. Note that e is a continuously differentiable and strictly monotone function ($\partial e/\partial p>0$ and $\partial e/\partial\rho<0$). The associated sound speed can be expressed as $c=\sqrt{\gamma\overline{p}/\rho}$, where $\overline{p}=p+B$. In the following, our analysis is based on the general EOS (2.3). Given this form of EOS, we can also express sound speed c in a general form of

$$c=\sqrt{\frac{p}{\rho^2 e_p}-\frac{e_\rho}{e_p}}. \tag{2.5}$$

3 Preliminaries

3.1 Solution structure of the multi-medium Riemann problem

For the multi-medium Riemann problem discussed in this paper, the solution structure is assumed to be very similar to that for a pure gas Riemann problem [32], if the existence of vacuum or phase transition is excluded. The solution structure in general consists of four constant regions connected by one of the three centered Riemann waves: two nonlinear waves (shock wave and rarefaction wave) and a linear wave (contact discontinuity or material interface). The two nonlinear waves are separated by the linear wave, as depicted in Fig. 1(a). In fact, these three waves are associated with three characteristic fields corresponding to the (right) eigenvectors $R^{(i)}$,$i=1,2,3$. Each wave family is shown along with the corresponding eigenvalue $u-c$, u or $u+c$.



(a) The general case in which two nonlinear Riemann waves are separated by the linear wave (interface)

(b) A particular case in which the left wave is a rarefaction and the right wave is a shock

Figure 1: Structure of the solution of a Riemann problem for 1D Euler equations.

In the following, we establish some relationships for different nonlinear waves. Rarefaction wave and shock wave in the Euler equations are associated with the $R^{(1)}$ and $R^{(3)}$ characteristic fields. See Fig. 1(b) for a particular case. If a rarefaction wave is generated in the left medium, via application of the generalized Riemann invariant through

https://doi.org/10.4208/cicp.190315.290316a Published online by Cambridge University Press

the rarefaction wave fan, we have

$$u-u_K=\int_{v_K}^{v}\rho c\mathrm{d}v, \tag{3.1}$$

where v is the specific volume and expressed as $v=1/\rho$. The subscript "K" refers to the initial state of the Riemann problem, which can be regarded as "L" or "R". (3.1) is also equivalent to

$$u-u_K=-\int_{p_K}^{p}\frac{1}{\rho c}\mathrm{d}p. \tag{3.2}$$

Similarly, for a right rarefaction wave we have

$$u-u_K=-\int_{v_K}^{v}\rho c\mathrm{d}v, \tag{3.3}$$

or

$$u-u_K=\int_{p_K}^{p}\frac{1}{\rho c}\mathrm{d}p. \tag{3.4}$$

Because the entropy s is constant for a rarefaction wave, thus we have

$$e-e_K=-\int_{v_K}^{v}p\mathrm{d}v, \tag{3.5}$$

according to the first law of thermodynamics $\mathrm{d}e=\mathrm{d}Q-p\mathrm{d}v$ and the expression for the change in entropy $\mathrm{d}s=\mathrm{d}Q/T$, where Q is the heat.

On the other hand, if the nonlinear wave is a shock wave we obtain

$$(u-u_K)^2=(p-p_K)(v_K-v), \tag{3.6}$$

and

$$e-e_K=\frac{1}{2}(p+p_K)(v_K-v), \tag{3.7}$$

using the shock wave relationship.

For the Riemann problem (2.1) with the general EOS (2.3), interfacial solutions of pressure p_I, velocity u_I and specific volume v_{IL}, v_{IR} are determined by the following system

$$\begin{cases} u_L-u_I=f(p_I,v_{IL},p_L,v_L), \\ u_I-u_R=f(p_I,v_{IR},p_R,v_R), \\ e(p_L,v_L)-e(p_I,v_{IL})=g(p_I,v_{IL},p_L,v_L), \\ e(p_I,v_{IR})-e(p_R,v_R)=-g(p_I,v_{IR},p_R,v_R), \end{cases} \tag{3.8}$$

according to (3.1)-(3.7). Here, the subscript "I" refers to the interface, and the subscript "IL" and "IR" denote the left and the right side of the interface, respectively. The functions f and g are respectively given by

$$f(p,v,p_K,v_K)=\begin{cases} \sqrt{(p-p_K)(v_K-v)}, & \text{if} \quad p>p_K, \\ -\displaystyle\int_{v_K}^{v}\rho c\mathrm{d}v, & \text{if} \quad p\le p_K, \end{cases} \tag{3.9}$$

https://doi.org/10.4208/cicp.190315.290316a Published online by Cambridge University Press

$$g(p,v,p_K,v_K)=\begin{cases}\dfrac{1}{2}(p+p_K)(v-v_K), & \text{if} \quad p>p_K,\\ \displaystyle\int_{v_K}^{v} p\mathrm{d}v, & \text{if} \quad p\leq p_K.\end{cases} \tag{3.10}$$

Given data p_K and ρ_K, we can easily obtain the following basic properties of f and g:

- f and g are both continuously differentiable functions of p and ρ.
- f is strictly monotone increasing for both p and ρ, i.e. $\partial f/\partial p>0$ and $\partial f/\partial\rho>0$.
- g is strictly monotone increasing for p and strictly monotone decreasing for ρ, i.e. $\partial g/\partial p>0$ and $\partial g/\partial\rho<0$.

3.2 Outline of the (modified) ghost fluid method

To simulate the multi-medium Riemann problem (2.1) and faithfully capture the wave structure in Section 3.1, the GFM is attractive. In a GFM-based algorithm for treating multi-fluid Euler-Euler coupling with an immiscible material interface, a narrow band of 3 to 5 grid points as ghost cells is defined in the vicinity of the material interface. At the ghost cells, ghost fluid and real fluid co-exist, as depicted in Fig. 2. Then, two separate single-medium Riemann problems (called GFM Riemann problems [17, 20]) need to be solved in the respective media with associated one-sided ghost fluid in each time step. One is in the left fluid medium with the initial conditions of

$$\frac{\partial U}{\partial t}+\frac{\partial F(U)}{\partial x}=0, \quad U|_{t=0}=\begin{cases}U_L, & x<x_0,\\ U_R^*, & x>x_0.\end{cases} \tag{3.11}$$

It solves from the grid node 1 on the left end to the ghost node next to the interface. The other is in the right medium with the initial conditions of

$$\frac{\partial U}{\partial t}+\frac{\partial F(U)}{\partial x}=0, \quad U|_{t=0}=\begin{cases}U_L^*, & x<x_0,\\ U_R, & x>x_0.\end{cases} \tag{3.12}$$

It solves from the ghost node next to the interface to the end node on the right. Hereafter, "$*$" indicates the ghost fluid (state). To compute the flow field at each time step, the central idea is the definition of ghost fluid states U_R^* and U_L^* corresponding to each phase of the interacting materials.

In the OGFM or GWGFM, the resolution of waves from the real-ghost interaction does not always provide correct and consistent Riemann waves in the respective real fluids [20]. When strong shocks impinging on interfaces with high impedance mismatch, this discrepancy in wave representation may lead to inaccurate shock and interface locations and result in unphysical numerical results in the real fluid region [17, 20]. To faithfully define ghost fluid state for the ghost cells, in the MGFM, a multi-medium Riemann problem is constructed along the normal direction of material interface. An approximate

https://doi.org/10.4208/cicp.190315.290316a Published online by Cambridge University Press

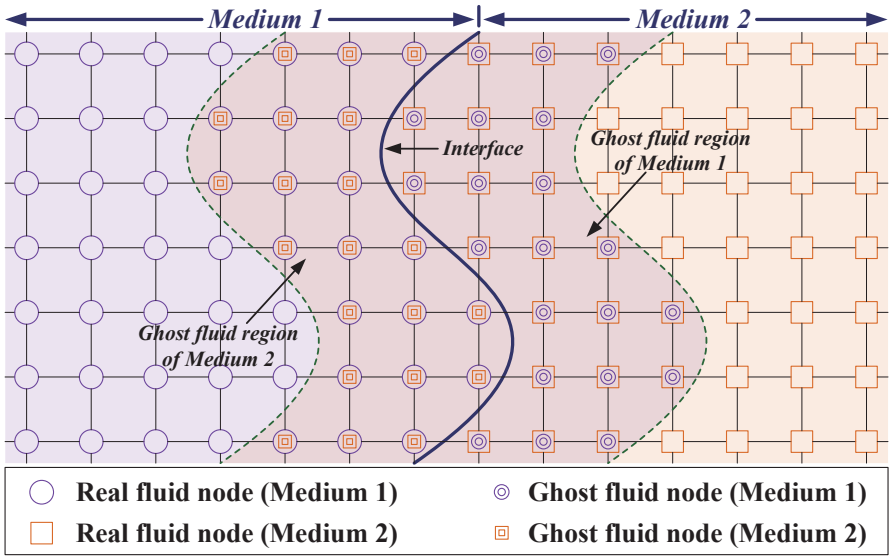


Figure 2: Distribution of the real fluid and the ghost fluid for multi-medium flows.

Riemann problem solver (ARPS) with a doubled-shock structure [33] is employed to predict the interfacial state. Then, the ghost fluid state U_R^* (U_L^*) is obtained by using the predicted interfacial state. Finally, we fix the real fluid density adjacent to the interface with the predicted interfacial entropy. The above demonstration can be seen in Fig. 3. More can be found in [17]. Thus, we can employ our favorite single-medium numerical solver to solve for each medium covering both the real fluid nodes and ghost fluid nodes next to the interface. By combining the solution for each medium according to the new interface location, we then obtain the overall solution valid for the whole computational domain at the new time step.

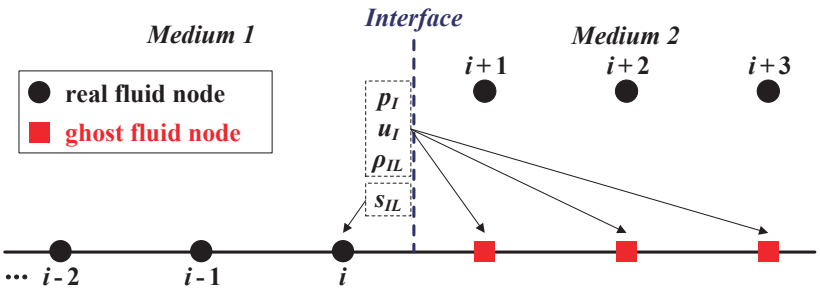


Figure 3: Illustration of the MGFM for defining the ghost fluid state of Medium 1.

https://doi.org/10.4208/cicp.190315.290316a Published online by Cambridge University Press

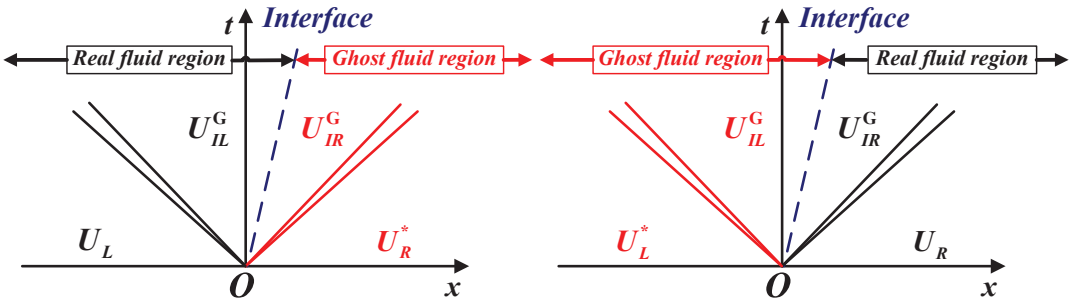
4 Exact definition of the ghost fluid state

Besides the above manner in the MGFM, in fact, there also exist other manners to define the ghost fluid state. The variety of exact ways to define the ghost fluid state does not affect the flow in the real fluid region. This will be systematically analyzed and discussed in this section.

4.1 Possible wave patterns in the ghost fluid region

We assume that one type of nonlinear Riemann waves (shock or rarefaction) is generated in the real fluid region. In the GFM, the ghost fluid states should be specially defined to make GFM Riemann problems (3.11) and (3.12) provided correct and consistent Riemann waves in the respective real fluids. For GFM Riemann problem (3.11), the ghost fluid state U_R^* should theoretically have the ability to make $U_{IL}^G = U_{IL}^e$. Similarly, the definition of U_L^* in (3.12) should have the ability to make $U_{IR}^G = U_{IR}^e$. On the other hand, the solution in the ghost fluid region, i.e. U_{IR}^G for (3.11) or U_{IL}^G for (3.12), is not our concern. See Fig. 4. Here, the superscript "G" indicates the exact state for GFM Riemann problem (3.11) or (3.12), and the superscript "e" indicates the exact state for original multi-medium Riemann problem (2.1).

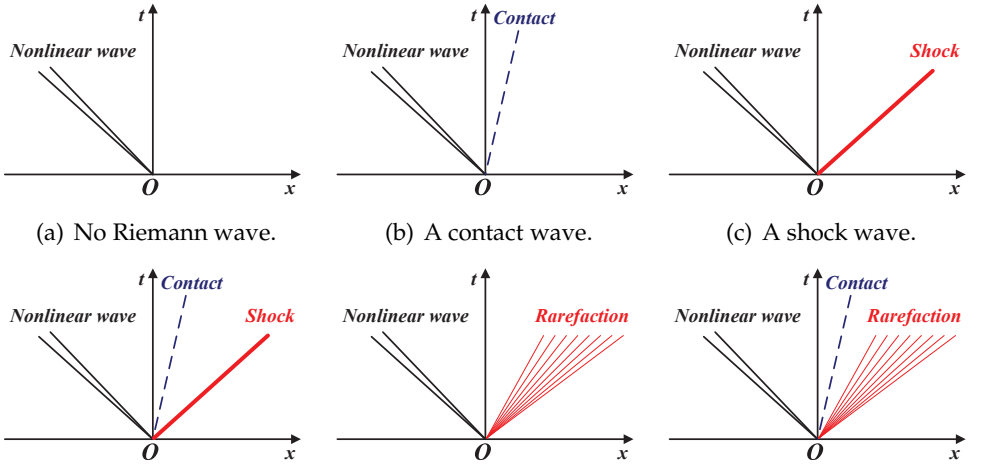
The ghost fluid region, including the interface separating the real fluid and the ghost fluid, only consists of six wave patterns: (1) no Riemann wave; (2) only a contact discontinuity; (3) only a shock wave; (4) a shock wave and a contact discontinuity; (5) only a rarefaction wave; (6) a rarefaction wave and a contact discontinuity, as depicted in Fig. 5. In the following, we present all relationships between the ghost fluid state and the interfacial state for different wave patterns in the ghost fluid region. Only in those cases, the Riemann wave in the real fluid for GFM Riemann problem (3.11) or (3.12) is definitely consistent with that for original Riemann problem (2.1). In other words, the "nonlinear wave" in Fig. 5 maintains the same wave pattern and solution structure as that for the original Riemann problem during the decomposition of the singularity.



(a) GFM Riemann problem (3.11) (b) GFM Riemann problem (3.12)

Figure 4: Real fluid region and ghost fluid region on x-t plane.

https://doi.org/10.4208/cicp.190315.290316a Published online by Cambridge University Press



(a) No Riemann wave. (b) A contact wave. (c) A shock wave.

(d) A shock wave and a contact wave. (e) A rarefaction wave. (f) A rarefaction wave and a contact wave.

Figure 5: Wave structures in the ghost fluid region for GFM Riemann problem (3.11).

Next, we study and derive expressions and conditions in detail for GFM Riemann problem (3.11). Table 1 lists all six symbols to denote each particular type of the solution. The left letter "W" stands for the wave generated in the real fluid region and the right letter specifies the wave type in the ghost fluid region (denoted by the superscript "$*$"): "S" or "R" respectively means that a shock wave or a rarefaction wave is generated in the ghost fluid region after the diaphragm is removed. If "S" or "R" is replaced by "$-$", it means that there is no Riemann wave in the ghost fluid region under special initial conditions. The middle symbol "$\vdots$" or "$|$" respectively denotes that there exists a trivial or a non-trivial contact discontinuity. The following analysis focuses on the GFM Riemann problem (3.11) with a general EOS (2.3). Similar conclusions can be drawn for GFM Riemann problem (3.12).

Table 1: Symbols of wave structure for GFM Riemann problem (3.11).

Category	1	2	3	4	5	6
Symbol	$W\vdots -^*$	$W\|-^*$	$W\vdots S^*$	$W\|S^*$	$W\vdots R^*$	$W\|R^*$

Category 1: No Riemann wave ($W\vdots -^*$). If the ghost fluid state for GFM Riemann problem (3.11) is defined as the exact state of Riemann problem (2.1) on the left side of the interface, no Riemann wave is generated in the ghost fluid region, as depicted in Fig. 5(a). In this case, the interface separating the real fluid and the ghost fluid can also be regarded as a trivial contact discontinuity, i.e. $p_{IL}^G = p_{IR}^G$, $v_{IL}^G = v_{IR}^G$, $u_{IL}^G = u_{IR}^G$. This definition of the ghost fluid state, similar to the MGFM treatment in Section 3.2, is uniquely determined

https://doi.org/10.4208/cicp.190315.290316a Published online by Cambridge University Press

by the interfacial state. The relationship can be expressed as $U_R^* = U_{IL}^e$, i.e.

$$p_R^* = p_I^e, \quad v_R^* = v_{IL}^e, \quad u_R^* = u_I^e. \tag{4.1}$$

Category 2: A contact wave ($W|-^*$). A contact wave is a discontinuous wave across which both pressure and velocity are constant but density or specific volume jumps discontinuously, i.e. $p_{IL}^G = p_{IR}^G$, $u_{IL}^G = u_{IR}^G$, $v_{IL}^G \neq v_{IR}^G$. Fig. 5(b) depicts a contact discontinuity. Hence, the pressure and the velocity of ghost fluid are necessarily defined as those at the interface. The density or the specific volume is chosen arbitrarily as long as the two data states U_{IL}^e and U_R^* are connected through a single jump discontinuity. The ghost fluid state can be defined as

$$p_R^* = p_I^e, \quad 0 < v_R^* \neq v_{IL}^e, \quad u_R^* = u_I^e. \tag{4.2}$$

Category 3: A shock wave ($W\!:\!S^*$). A shock wave, see Fig. 5(c), is identified by the condition that pressure is increased across a shock front. Other quantities, such as v and u, also change across a shock wave. Application of the Rankine-Hugoniot conditions and EOS (2.3) yields the following relations of interest:

$$\begin{cases} \sqrt{(p_I^e - p_R^*)(v_R^* - v_{IL}^e)} + u_R^* - u_I^e = 0, \\ e(p_I^e, v_{IL}^e) - e(p_R^*, v_R^*) = \dfrac{1}{2}(p_I^e + p_R^*)(v_R^* - v_{IL}^e), \\ p_R^* < p_I^e. \end{cases} \tag{4.3}$$

Category 4: A shock wave and a contact wave ($W|S^*$). As shown in Fig. 5(d), a shock wave and a contact wave separate three constant states. The pressure and velocity between the contact and the shock are exactly equal to the interfacial quantities, and the density or the specific volume is arbitrary but not equal to the exact value on the left side of the interface. Then, application of the Rankine-Hugoniot conditions and EOS (2.3) for the two states across the shock yields the following relations of interest:

$$\begin{cases} \sqrt{(p_I^e - p_R^*)(v_R^* - v^{\text{arb}})} + u_R^* - u_I^e = 0, \\ e(p_I^e, v^{\text{arb}}) - e(p_R^*, v_R^*) = \dfrac{1}{2}(p_I^e + p_R^*)\left(v_R^* - v^{\text{arb}}\right), \\ p_R^* < p_I^e, \quad 0 < v^{\text{arb}} \neq v_{IL}^e. \end{cases} \tag{4.4}$$

Category 5: A rarefaction wave ($W\!:\!R^*$). A rarefaction wave, see Fig. 5(e), is identified by the condition that pressure is decreased through a rarefaction wave fan. Other quantities, such as v and u, also change across a rarefaction wave. This wave has a fan-type shape and is enclosed by two bounding characteristics corresponding to the head and the tail of the wave. Application of the Generalised Riemann Invariants and EOS (2.3) yields

https://doi.org/10.4208/cicp.190315.290316a Published online by Cambridge University Press

the following relations of interest:

$$\begin{cases} -\int_{v_R^*}^{v_{IL}^e} \rho c \mathrm{d}v + u_R^* - u_I^e = 0, \\ e(p_I^e, v_{IL}^e) - e(p_R^*, v_R^*) = -\int_{v_R^*}^{v_{IL}^e} p \mathrm{d}v, \\ p_R^* > p_I^e. \end{cases} \tag{4.5}$$

Category 6: A rarefaction wave and a contact wave ($W|R^*$). As shown in Fig. 5(f), a rarefaction wave and a contact wave separate three constant states, excluding the state inside the rarefaction fan. The pressure and velocity between the contact and the tail of the rarefaction are exactly equal to the interfacial quantities, and the density or the specific volume is arbitrary but not equal to the exact value on the left side of the interface. Then, application of the Generalised Riemann Invariants and EOS (2.3) for the two states across the rarefaction yields the following relations of interest:

$$\begin{cases} -\int_{v_R^*}^{v^{\mathrm{arb}}} \rho c \mathrm{d}v + u_R^* - u_I^e = 0, \\ e(p_I^e, v^{\mathrm{arb}}) - e(p_R^*, v_R^*) = -\int_{v_R^*}^{v^{\mathrm{arb}}} p \mathrm{d}v, \\ p_R^* > p_I^e, \quad 0 < v^{\mathrm{arb}} \neq v_{IL}^e. \end{cases} \tag{4.6}$$

4.2 Validation by numerical simulations

In this section, we give some numerical tests to validate the above analysis. Without loss of generality, we construct and solve a set of multi-medium Riemann problems with EOS (2.4). Depending on the interfacial state (i.e. p_I^e, ρ_{IL}^e, u_I^e), which is obtained by exactly solving the multi-medium Riemann problem (2.1), the ghost fluid state of GFM Riemann problem (3.11) is defined as follows (The ghost fluid state of GFM Riemann problem (3.12) can be defined similarly):

Category 1: No Riemann wave ($W\vdots -^*$). Once the interfacial state is obtained, the ghost fluid quantities p_R^*, v_R^* (ρ_R^*), u_R^* can be set as (4.1).

Category 2: A contact wave ($W|-^*$). Once the interfacial state is obtained, the ghost fluid quantities p_R^*, v_R^* (ρ_R^*), u_R^* can be set as (4.2), especially v_R^* is arbitrary, as long as $v_R^* > 0$ and $v_R^* \neq v_{IL}^e$.

Category 3: A shock wave ($W\vdots S^*$). Once the interfacial state is obtained, the ghost fluid pressure p_R^* can be set to make $p_R^* < p_I^e$. The ghost fluid density ρ_R^* and velocity u_R^* can be determined respectively from

$$\rho_R^* = \rho_{IL}^e \left[\frac{\gamma_L - 1}{\gamma_L + 1} \frac{\overline{p}_I^e}{\overline{p}_R^*} + 1 \right] \Big/ \left[\frac{\overline{p}_I^e}{\overline{p}_R^*} + \frac{\gamma_L - 1}{\gamma_L + 1} \right], \tag{4.7}$$

https://doi.org/10.4208/cicp.190315.290316a Published online by Cambridge University Press

and

$$u_R^*=u_I^e-(p_I^e-p_R^*)\sqrt{\left[\frac{2}{(\gamma_L+1)\rho_{IL}^e}\right]\Big/\left[\frac{\gamma_L-1}{\gamma_L+1}\overline{p}_I^e+\overline{p}_R^*\right]}. \tag{4.8}$$

Category 4: A shock wave and a contact wave ($W|S^*$). Once the interfacial state is obtained, the ghost fluid pressure p_R^* can be set to make $p_R^*<p_I^e$. The ghost fluid density ρ_R^* and velocity u_R^* can be determined respectively from

$$\rho_R^*=\rho^{\text{arb}}\left[\frac{\gamma_L-1}{\gamma_L+1}\frac{\overline{p}_I^e}{\overline{p}_R^*}+1\right]\Big/\left[\frac{\overline{p}_I^e}{\overline{p}_R^*}+\frac{\gamma_L-1}{\gamma_L+1}\right], \tag{4.9}$$

and

$$u_R^*=u_I^e-(p_I^e-p_R^*)\sqrt{\left[\frac{2}{(\gamma_L+1)\rho^{\text{arb}}}\right]\Big/\left[\frac{\gamma_L-1}{\gamma_L+1}\overline{p}_I^e+\overline{p}_R^*\right]}. \tag{4.10}$$

As noted in (4.4), ρ^{arb} is arbitrary, as long as $\rho^{\text{arb}}>0$ and $\rho^{\text{arb}}\neq\rho_{IL}^e$.

Category 5: A rarefaction wave ($W\vdots R^*$). Once the interfacial state is obtained, the ghost fluid pressure p_R^* can be set to make $p_R^*>p_I^e$. The ghost fluid density ρ_R^* and velocity u_R^* can be determined respectively from

$$\rho_R^*=\rho_{IL}^e\left(\frac{\overline{p}_R^*}{\overline{p}_I^e}\right)^{\frac{1}{\gamma_L}}, \tag{4.11}$$

and

$$u_R^*=u_I^e-\frac{2c_{IL}^e}{\gamma_L-1}\left[1-\left(\frac{\overline{p}_R^*}{\overline{p}_I^e}\right)^{\frac{\gamma_L-1}{2\gamma_L}}\right]. \tag{4.12}$$

Category 6: A rarefaction wave and a contact wave ($W|R^*$). Once the interfacial state is obtained, the ghost fluid pressure p_R^* can be set to make $p_R^*>p_I^e$. The ghost fluid density ρ_R^* and velocity u_R^* can be determined respectively from

$$\rho_R^*=\rho^{\text{arb}}\left(\frac{\overline{p}_R^*}{\overline{p}_I^e}\right)^{\frac{1}{\gamma_L}}, \tag{4.13}$$

and

$$u_R^*=u_I^e-\frac{2c^{\text{arb}}}{\gamma_L-1}\left[1-\left(\frac{\overline{p}_R^*}{\overline{p}_I^e}\right)^{\frac{\gamma_L-1}{2\gamma_L}}\right]. \tag{4.14}$$

Here, $c^{\text{arb}}=\sqrt{\gamma\overline{p}/\rho^{\text{arb}}}$. As noted in (4.6), ρ^{arb} is arbitrary, as long as $\rho^{\text{arb}}>0$ and $\rho^{\text{arb}}\neq\rho_{IL}^e$.

We take an air-water Riemann problem as an example to validate the above definitions of the ghost fluid state. The initial non-dimensional conditions are

$$\begin{cases} x<0.5: & (\gamma_L,B_L,\rho_L,u_L,p_L)=(1.4,0.0,0.7,-80.0,8000.0),\\ x>0.5: & (\gamma_R,B_R,\rho_R,u_R,p_R)=(7.15,3309.0,1.0,0.0,1.0). \end{cases} \tag{4.15}$$

https://doi.org/10.4208/cicp.190315.290316a Published online by Cambridge University Press

In this problem, a left rarefaction wave and a right shock wave are generated in respective media. Fig. 6 depicts the pressure, velocity and density profiles at $t=1.5\times10^{-3}$ for different media including ghost fluid regions. In this figure, the exact solution is obtained by exactly solving the multi-medium Riemann problem (2.1). Other results for comparison are obtained by the following steps: (1) Respectively define ghost fluid states U_R^* and U_L^* for GFM Riemann problems (3.11) and (3.12) as the manners above. (2) Exactly solve these single-medium GFM Riemann problems for the air and the water medium. Although the wave patterns in the ghost fluid region are different, the results in the real fluid region are exactly the same as the exact solution.

5 A practical GFM

As analyzed above, there theoretically exist various possible choices to define the ghost fluid state, as long as one of six conditions in Section 4 is satisfied. However, the definition of ghost fluid state is highly relevant to wave structures in the ghost fluid region. This is sometimes not convenient to be performed in practice. In the following, we present some simple and effective ways to define the ghost fluid state.

5.1 Prediction of the interfacial state

In order to find a useful way in practical applications, we firstly draw a lemma.

Lemma 5.1. *Let $X=(x_1,x_2,\cdots,x_n)\in D\subset\mathbb{R}^n$. Suppose $f_i:D\to\mathbb{R}, i=1,2,\cdots,n$, be continuously differentiable functions and*

$$\frac{\partial(f_1,f_2,\cdots,f_n)}{\partial(x_1,x_2,\cdots,x_n)}\neq 0.$$

If there are two elements X_1 and X_2 of D such that $f_i(X_1)=f_i(X_2)$ for $i=1,2,\cdots,n$, then $X_1=X_2$.

An equivalent conclusion of Lemma 5.1 is that the solution to nonlinear equations $f_i(X)=A_i$ for $i=1,2,\cdots,n$ is unique, where each A_i is a constant. This is easily proved with the property of function f_i. From Lemma 5.1, we have the following important theorem.

Theorem 5.1. *For the multi-medium Riemann problem* (2.1) *with a general EOS* (2.3) *where $\partial e/\partial p>0$ and $\partial e/\partial\rho<0$, if one interfacial quantity is predicted correctly using the ghost fluid method, then other interfacial quantities are also exact. That is, the following conclusions are held for GFM Riemann problem* (3.11)*:*

(1) if $u_I^G=u_I^e$, then $p_I^G=p_I^e$, $\rho_{IL}^G=\rho_{IL}^e$,

(2) if $p_I^G=p_I^e$, then $\rho_{IL}^G=\rho_{IL}^e$, $u_I^G=u_I^e$,

(3) if $\rho_{IL}^G=\rho_{IL}^e$, then $u_I^G=u_I^e$, $p_I^G=p_I^e$.

https://doi.org/10.4208/cicp.190315.290316a Published online by Cambridge University Press

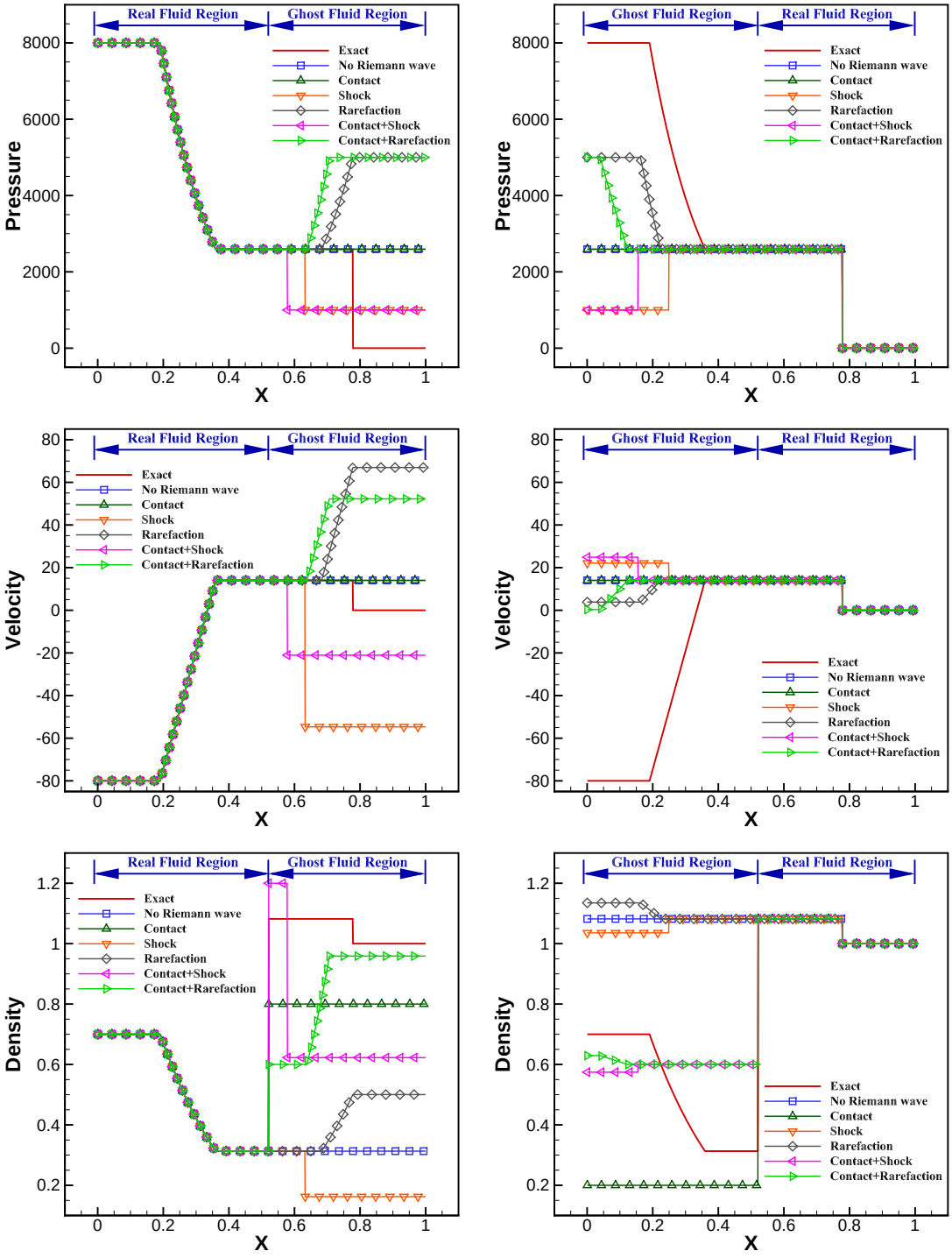


Figure 6: Comparison of different definitions of the ghost fluid state. Top: Pressure; Middle: Velocity; Bottom: Density. Left: Air medium; Right: Water medium.

https://doi.org/10.4208/cicp.190315.290316a Published online by Cambridge University Press

The following conclusions are held for GFM Riemann problem (3.12)*:*

(4) if $u_I^G = u_I^e$*, then* $p_I^G = p_I^e$, $\rho_{IR}^G = \rho_{IR}^e$,

(5) if $p_I^G = p_I^e$*, then* $\rho_{IR}^G = \rho_{IR}^e$, $u_I^G = u_I^e$,

(6) if $\rho_{IR}^G = \rho_{IR}^e$*, then* $u_I^G = u_I^e$, $p_I^G = p_I^e$.

Proof. According to (3.8), the states on the left side of the interface for multi-medium Riemann problem (2.1) are determined by the following system of nonlinear equations

$$u_L - u_I^e = f_1(p_I^e, \rho_{IL}^e, p_L, \rho_L), \tag{5.1a}$$
$$e(p_L, \rho_L) - e(p_I^e, \rho_{IL}^e) = g_1(p_I^e, \rho_{IL}^e, p_L, \rho_L). \tag{5.1b}$$

On the other hand, the states on the left side of the interface for single-medium GFM Riemann problem (3.11) are determined by the following system of nonlinear equations

$$u_L - u_I^G = f_2(p_I^G, \rho_{IL}^G, p_L, \rho_L), \tag{5.2a}$$
$$e(p_L, \rho_L) - e(p_I^G, \rho_{IL}^G) = g_2(p_I^G, \rho_{IL}^G, p_L, \rho_L). \tag{5.2b}$$

In (5.1) and (5.2), functions f_1, f_2 and g_1, g_2 are respectively given by the expressions for f and g in (3.9) and (3.10).

First of all, we shall show that $f_1 = f_2$ and $g_1 = g_2$, if one interfacial quantity (i.e. u_I^G, p_I^G or ρ_{IL}^G) is predicted correctly. Under the assumption of $u_I^e < u_L$ or $p_I^e > p_L$ or $\rho_{IL}^e > \rho_L$, there is a shock wave on the left side of the material interface. It should be noted that the left state U_L in multi-medium Riemann problem (2.1) is the same as that in single-medium GFM Riemann problem (3.11). That is to say, if one interfacial quantity is predicted correctly (i.e. $u_I^G = u_I^e$ or $p_I^G = p_I^e$ or $\rho_{IL}^G = \rho_{IL}^e$), the wave on the same side for single-medium GFM Riemann problem (3.11) is also a shock wave. Likewise, the waves are both rarefaction waves under another opposite assumption of $u_I^e > u_L$ or $p_I^e < p_L$ or $\rho_{IL}^e < \rho_L$. This means that the wave patterns on the left side are always identical for multi-medium Riemann problem (2.1) and GFM Riemann problem (3.11), and therefore we can replace f_1 and f_2 by f and replace g_1 and g_2 by g in the following.

Next, we shall show that conclusions (1)–(3) are held:

(1) Comparison of (5.1a) and (5.2a) and comparison of (5.1b) and (5.2b) with $u_I^G = u_I^e$ give

$$\begin{cases} f(p_I^G, \rho_{IL}^G, p_L, \rho_L) = f(p_I^e, \rho_{IL}^e, p_L, \rho_L), \\ e(p_I^G, \rho_{IL}^G) + g(p_I^G, \rho_{IL}^G, p_L, \rho_L) = e(p_I^e, \rho_{IL}^e) + g(p_I^e, \rho_{IL}^e, p_L, \rho_L). \end{cases} \tag{5.3}$$

Set $\bar{p}(x,y) = f(x,y,p_L,\rho_L)$ and $\bar{q}(x,y) = e(x,y) + g(x,y,p_L,\rho_L)$. It is easily found that $\partial\bar{p}/\partial x > 0$, $\partial\bar{p}/\partial y > 0$, $\partial\bar{q}/\partial x > 0$ and $\partial\bar{q}/\partial y < 0$ according to the properties of f and g and the assumption on EOS (2.3). This further implies that $\partial(\bar{p},\bar{q})/\partial(x,y) < 0$. By applying Lemma 5.1, we have $p_I^G = p_I^e$ and $\rho_{IL}^G = \rho_{IL}^e$. Consequently, the conclusion (1) is held.

https://doi.org/10.4208/cicp.190315.290316a Published online by Cambridge University Press

(2) Comparison of (5.1b) and (5.2b) with $p_I^G = p_I^e$ gives

$$e(p_I^e,\rho_{IL}^G)+g(p_I^e,\rho_{IL}^G,p_L,\rho_L)=e(p_I^e,\rho_{IL}^e)+g(p_I^e,\rho_{IL}^e,p_L,\rho_L). \tag{5.4}$$

Set $\bar{p}(x)=e(p_I^e,x)+g(p_I^e,x,p_L,\rho_L)$. It is easily found that $\partial\bar{p}/\partial x<0$ according to the property of g and the assumption on EOS (2.3). By applying Lemma 5.1, we have $\rho_{IL}^G=\rho_{IL}^e$. Further comparison of (5.1a) and (5.2a) gives

$$u_I^G+f(p_I^G,\rho_{IL}^G,p_L,\rho_L)=u_I^e+f(p_I^e,\rho_{IL}^e,p_L,\rho_L). \tag{5.5}$$

Substitution of $p_I^G=p_I^e$ and $\rho_{IL}^G=\rho_{IL}^e$ into (5.5) yields $u_I^G=u_I^e$. Consequently, the conclusion (2) is held.

(3) The conclusion (3) can be proved similarly as in (2).

As for GFM Riemann problem (3.12), we can show that conclusions (4)–(6) are also held in a similar way. The theorem is thus proved. □

5.2 Practical techniques for defining the ghost fluid state

The above theorem indicates a way to define the ghost fluid state in practice. Without loss of generality, we also take the GFM Riemann problem (3.11) as an example to illustrate this methodology. The aim is to adjust p_R^*, ρ_R^* and u_R^* to make $u_I^G=u_I^e$ (or $p_I^G=p_I^e$ or $\rho_{IL}^G=\rho_{IL}^e$). There exist at least two simple but effective approaches, as we shall see.

Approach A. An expression for the velocity solution u_I^G at the interface is

$$u_I^G=u_R^*+f(p_I^G,\rho_{IR}^G,p_R^*,\rho_R^*). \tag{5.6}$$

If $p_R^*=p_I^G$ (or $\rho_R^*=\rho_{IR}^G$), (5.6) can be simplified to $u_I^G=u_R^*$. The requirement of $u_I^G=u_I^e$ implies $u_R^*=u_I^e$ for the definition of velocity in the ghost fluid region. According to Theorem 5.1, $p_I^G=p_I^e$ and $\rho_{IL}^G=\rho_{IL}^e$ are then automatically satisfied for the GFM Riemann problem (3.11). As a result, one definition of the ghost fluid state can be written as

$$p_R^*=p_I^e,\rho_R^*=\rho_{IL}^e,u_R^*=u_I^e, \tag{5.7}$$

which implies that there is no Riemann wave in the ghost fluid region, as the solution type $W\vdots-^*$ in Section 4. Another definition of the ghost fluid state can be written as

$$p_R^*=p_I^e,\quad \rho_R^*\neq\rho_{IL}^e,\quad u_R^*=u_I^e, \tag{5.8}$$

which implies that there is a contact wave in the ghost fluid region, as the solution type $W|-^*$ in Section 4.

Obviously, there is no big difference between (5.7) and (5.8) for the definition of the ghost fluid state. The assumption of no Riemann wave structure in the ghost fluid region is a simple and effective manner to treat multi-medium flows. Therefore, we regard (5.7) as the representation of Approach A.

https://doi.org/10.4208/cicp.190315.290316a Published online by Cambridge University Press

Approach B. Another expression for the velocity solution u_I^G at the interface is

$$u_I^G=\frac{1}{2}(u_L+u_R^*)+\frac{1}{2}\left[f(p_I^G,\rho_{IR}^G,p_R^*,\rho_R^*)-f(p_I^G,\rho_{IL}^G,p_L,\rho_L)\right]. \tag{5.9}$$

If $p_R^*=p_L$ and $\rho_R^*=\rho_L$, there is no contact discontinuity for the GFM Riemann problem (3.11) and so $\rho_{IR}^G=\rho_{IL}^G$. (5.9) can then be simplified to $u_I^G=\frac{1}{2}(u_L+u_R^*)$. The requirement of $u_I^G=u_I^e$ implies $u_R^*=2u_I^e-u_L$. According to Theorem 5.1, $p_I^G=p_I^e$ and $\rho_{IL}^G=\rho_{IL}^e$ are then automatically satisfied for the GFM Riemann problem (3.11). As a result, we have the following definition

$$p_R^*=p_L,\quad \rho_R^*=\rho_L,\quad u_R^*=2u_I^e-u_L. \tag{5.10}$$

Table 2 shows all the definitions of the ghost fluid states for GFM Riemann problems (3.11) and (3.12). In this table, "RP" means Riemann problem. Further comparison of Approach A and Approach B gives the following properties:

- There is no nonlinear wave in the ghost fluid region using Approach A, and there is always a mirrored wave structure as in the real fluid using Approach B;
- Three interfacial quantities (i.e. p_I, u_I and ρ_{IL}(or ρ_{IR})) are required to define the ghost fluid state using Approach A, and only one interfacial quantity (i.e. u_I) is required using Approach B.

Table 2: Practical definitions of the ghost fluid states.

Approach	GFM RP (3.11)			GFM RP (3.12)		
	p_R^*	ρ_R^*	u_R^*	p_L^*	ρ_L^*	u_L^*
A	p_I^e	ρ_{IL}^e	u_I^e	p_I^e	ρ_{IR}^e	u_I^e
B	p_L	ρ_L	$2u_I^e-u_L$	p_R	ρ_R	$2u_I^e-u_R$

As a matter of fact, Approach A is the basic idea of MGFM, which is shown in Section 3.2. In contrast with Approach A, Approach B provides a more simple and meaningful way for the GFM, in which only one degree of freedom contributes to the definition of the ghost fluid state. Approach B enables the pressure and density to be symmetrically copied from the real fluid on the other side of the interface onto the ghost field. The interfacial velocity, as the unique degree of freedom, is utilized to compute the velocity for the ghost points. This treatment is similar to the reflective boundary condition. An essential prerequisite is the fact that the interfacial velocity must be solved or predicted exactly. It implies that the reflective boundary condition is correct when applied to moving boundary problems where the wall moves with a prescribed speed. Moreover, it further proves that the reflective boundary condition used in conjunction with exact interfacial velocity is also a reasonable choice in simulating multi-medium flows or fluid-structure coupling problems.

It should be noted that there are other approaches to define the ghost fluid state. For example, we can set $u_R^*=u_L$ for the GFM Riemann problem (3.11). Then the wave

https://doi.org/10.4208/cicp.190315.290316a Published online by Cambridge University Press

structure in the ghost fluid region is different from that in the real fluid region. Clearly, p_R^* and ρ_R^* can be determined according to (5.6), which is related to the expression of f in (3.9). This approach requires two interfacial quantities (i.e. p_I and ρ_{IL}) to define the ghost fluid state, but seems too complicated to be used in practice.

5.3 A practical algorithm in numerical simulations

Approach B provides us another feasible algorithm to simulate the multi-medium flows. This algorithm is simple and different from the MGFM, and does also not affect the flow in the real fluid region theoretically.

For one-dimensional case, the pressure and density of the ghost fluid can be simply defined by constantly extrapolating the corresponding quantities of the real fluid, i.e. $p^*=p_{real}$, $\rho^*=\rho_{real}$, while the velocity of the ghost fluid can be defined as $u^*=2u_I-u_{real}$, as shown in Fig. 7. We call this GFM the practical GFM (PGFM) in this paper. The PGFM is similar to the reflective boundary condition for an impermeable wall. In this way, the wave structure in the ghost fluid region is theoretically identical to that in the real fluid region, which can only be a shock or a rarefaction. Here, u_I is the velocity of material interface and obtained by solving the multi-medium Riemann problem. It is clear that the use of an exact Riemann problem solver would be often time-consuming, especially in multi-dimension. So the use of an ARPS will become necessary. The ARPS adopted here is also based on a doubled-shock structure as in the MGFM, which can be written as

$$\begin{cases} u_L-u_I^a=\sqrt{(p_I^a-p_L)\left(\dfrac{1}{\rho_L}-\dfrac{1}{\rho_{IL}^a}\right)}, \\ u_I^a-u_R=\sqrt{(p_I^a-p_R)\left(\dfrac{1}{\rho_R}-\dfrac{1}{\rho_{IR}^a}\right)}, \\ e(p_L,\rho_L)-e(p_I^a,\rho_{IL}^a)=\dfrac{1}{2}(p_I^a+p_L)\left(\dfrac{1}{\rho_{IL}^a}-\dfrac{1}{\rho_L}\right), \\ e(p_I^a,\rho_{IR}^a)-e(p_R,\rho_R)=-\dfrac{1}{2}(p_I^a+p_R)\left(\dfrac{1}{\rho_{IR}^a}-\dfrac{1}{\rho_R}\right). \end{cases} \tag{5.11}$$

Here the superscript "a" denotes an approximation to the exact state. u_I is set to the velocity solution u_I^a of (5.11). More specifically, for gas-water Riemann problems with EOS (2.4), u_I^a is obtained from

$$\begin{cases} u_L-u_I^a=(p_I^a-p_L)\sqrt{\left[\dfrac{2}{(\gamma_L+1)\rho_L}\right]\Big/\left[(p_I^a+B_L)+\dfrac{\gamma_L-1}{\gamma_L+1}(p_L+B_L)\right]}, \\ u_I^a-u_R=(p_I^a-p_R)\sqrt{\left[\dfrac{2}{(\gamma_R+1)\rho_R}\right]\Big/\left[(p_I^a+B_R)+\dfrac{\gamma_R-1}{\gamma_R+1}(p_R+B_R)\right]}. \end{cases} \tag{5.12}$$

https://doi.org/10.4208/cicp.190315.290316a Published online by Cambridge University Press

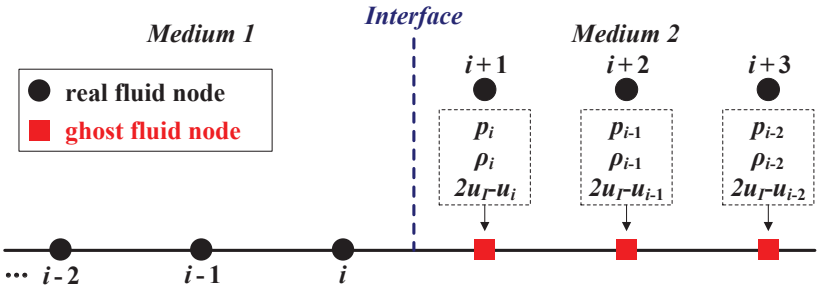


Figure 7: Illustration of the PGFM for defining the ghost fluid state of Medium 1.

Obviously, by using this Riemann-problem-based technique in the normal direction of the interface, the PGFM can be easily implemented for multi-dimension. The extension of this technique to two-dimensional systems is done via projecting the velocity field into the normal and tangential directions of the interface. The PGFM are then implemented along the normal direction as for the one-dimensional case, while the tangential velocity of ghost fluid is simply handled by extrapolation. This multi-dimensional treatment is similar to that in the MGFM [17]. Here we briefly summarize the general procedure of the PGFM algorithm:

1 Advance the interface (e.g. via using level set technique) to a new time step, and get the new interface location.

2 Predict the interfacial velocity by solving coupled equations (5.11), and then define ghost fluid states as the implement in Fig. 7.

3 Choose a suitable high-order single medium scheme to solve for each fluid medium. In that way the solution in all the media is advanced to the new time step.

4 Obtain the final solution over whole computation domain according to the new interface location, and then update the new time step size and proceed to the next time step.

5.4 Accuracy of the PGFM

The interface accuracy and local conservation error of MGFM can achieve "third-order accuracy" in the sense of comparing to the exact solution of the multi-medium Riemann problem [30]. The PGFM, with a different definition of the ghost fluid state, seems to have a similar performance in multi-medium flows simulations. Now, we analyze the accuracy of the PGFM when applied to the Riemann problem (2.1). It should be noted that the "accuracy" discussed here means how accurate the boundary conditions are implicitly imposed at the material interface and how accurate the interface states are approximated by the PGFM technique, which is in contrast with the accuracy of the numerical scheme or the errors between the exact solution and the numerical solution.

https://doi.org/10.4208/cicp.190315.290316a Published online by Cambridge University Press

We firstly establish some formula to estimate the interface state. Evaluation of the integrals in (3.1) and (3.2) via using the 2-point closed Newton-Cotes formula (trapezoidal rule) gives

$$u-u_K=-\frac{1}{2}(\rho c+\rho_K c_K)(v_K-v)+\mathcal{O}(v-v_K)^3, \tag{5.13}$$

$$u-u_K=-\frac{1}{2}\left(\frac{1}{\rho c}+\frac{1}{\rho_K c_K}\right)(p-p_K)+\mathcal{O}(p-p_K)^3. \tag{5.14}$$

Multiplication of (5.13) by (5.14) and manipulation with the fact that ρ and c are both continuous and differentiable functions of p lead to

$$(u-u_K)^2=(p-p_K)(v_K-v)+\mathcal{O}(p-p_K)^3, \tag{5.15}$$

A similar result for a right rarefaction can also be obtained. On the other hand, the isentropic relation (3.5) can be evaluated by

$$e-e_K=\frac{1}{2}(p+p_K)(v_K-v)+\mathcal{O}(v-v_K)^3. \tag{5.16}$$

Comparison of (3.6), (3.7), (5.15) and (5.16) gives the following expression

$$u_I^a=u_I^e+\mathcal{O}[max(|p_I^e-p_L|,|p_I^e-p_R|)]^3, \tag{5.17}$$

which means the velocity u_I^a provided by ARPS (5.11) approximates the exact interfacial velocity u_I^e to third-order accuracy regardless of the solution type. It is easily seen that other quantities, such as p_I^a, ρ_{IL}^a and ρ_{IR}^a, also have similar results.

Lemma 5.2. *The following interface error estimates are held for the respective GFM Riemann problems* (3.11) *and* (3.12) *using the PGFM with ARPS* (5.11)*:*

$$\begin{aligned}
&(1)\quad p_I^{P1}-p_I^e=\mathcal{O}(p_I^e-p_L)^3, && (4)\quad p_I^{P2}-p_I^e=\mathcal{O}(p_I^e-p_R)^3,\\
&(2)\quad u_I^{P1}-u_I^e=\mathcal{O}(p_I^e-p_L)^3, && (5)\quad u_I^{P2}-u_I^e=\mathcal{O}(p_I^e-p_R)^3,\\
&(3)\quad \rho_{IL}^{P1}-\rho_{IL}^e=\mathcal{O}(p_I^e-p_L)^3, && (6)\quad \rho_{IR}^{P2}-\rho_{IR}^e=\mathcal{O}(p_I^e-p_R)^3,
\end{aligned}$$

where $p_I^{P1}(p_I^{P2})$, $u_I^{P1}(u_I^{P2})$ *and* $\rho_{IL}^{P1}(\rho_{IR}^{P2})$ *are the exact interfacial pressure, velocity and density of the GFM Riemann problem* (3.11)((3.12)) *using the PGFM.*

Proof. According to (3.8), any interfacial quantity (i.e. p_I, u_I or ρ_{IL}) of GFM Riemann problem (3.11) is determined by all the left and the right initial flow states (i.e. p_L, u_L, ρ_L and p_R^*, u_R^*, ρ_R^*). With the definition of $p_R^*=p_L$, $u_R^*=2u_I-u_L$, $\rho_R^*=\rho_L$, these interfacial quantities can be expressed as

$$q_I=h_q(p_L,u_L,\rho_L,p_L,2u_I-u_L,\rho_L), \tag{5.18}$$

https://doi.org/10.4208/cicp.190315.290316a Published online by Cambridge University Press

where q_I denotes p, u, ρ at the left side of the interface. Substitution of $u_I = u_I^e$ into (5.18) yields

$$q_I^G = h_q(p_L, u_L, \rho_L, p_L, 2u_I^e - u_L, \rho_L). \tag{5.19}$$

Substitution of $u_I = u_I^a$ into (5.18) and use of (5.17) and Taylor's series expansion give

$$q_I^P = h_q(p_L, u_L, \rho_L, p_L, 2u_I^e - u_L, \rho_L) + \mathcal{O}(p_I^e - p_L)^3. \tag{5.20}$$

Subtraction of (5.19) from (5.20) and use of $q_I^G = q_I^e$ from Section 5.2 directly lead to the satisfaction of error estimates (1)–(3). In a similar way, we can show the error estimates (4)–(6) are also held for the GFM Riemann problem (3.12) when the PGFM is employed. □

Lemma 5.3. *The following conservation error estimates are held using the PGFM with ARPS* (5.11)*:*

$$(1) \quad CEL = \mathcal{O}(p_I^e - p_L)^3,$$
$$(2) \quad CER = \mathcal{O}(p_I^e - p_R)^3,$$
$$(3) \quad CET = \mathcal{O}[max(|p_I^e - p_L|, |p_I^e - p_R|)]^3,$$

where CEL, CER, and CET are the conservation errors for the medium on the left- and right-hand side of the interface and over the whole computational domain, respectively.

Proof. Assume that the interface location x_I is between x_A and x_B. By applying the integral conservation law to the GFM Riemann problem (3.11) over interval $[x_A, x_I]$, to the GFM Riemann problem (3.12) over interval $[x_I, x_B]$, and to the Riemann problem (2.1) over interval $[x_A, x_B]$ from time t^n to t^{n+1}, CEL, CER, and CET are respectively represented as

$$CEL = \frac{1}{\Delta t}\left[\int_{x_A}^{x_I^{n+1}} U^{n+1}dx - \int_{x_A}^{x_I^n} U^n dx + \int_{t^n}^{t^{n+1}} (F_{IL} - u_I U_{IL} - F_A)dt\right], \tag{5.21}$$

$$CER = \frac{1}{\Delta t}\left[\int_{x_I^{n+1}}^{x_B} U^{n+1}dx - \int_{x_I^n}^{x_B} U^n dx + \int_{t^n}^{t^{n+1}} (F_B - F_{IR} + u_I U_{IR})dt\right], \tag{5.22}$$

$$CET = \frac{1}{\Delta t}\left[\int_{x_A}^{x_B} U^{n+1}dx - \int_{x_A}^{x_B} U^n dx + \int_{t^n}^{t^{n+1}} (F_B - F_A)dt\right]. \tag{5.23}$$

Theoretically, CEL, CER and CET should be equal to zero because of conservation laws. For the conservation error CEL using the PGFM, we split the first integral in (5.21) into two integrals, namely

$$\int_{x_A}^{x_I^{n+1}} U^{n+1,P1}dx = \int_{x_A}^{x_I^{n+1}} U^{n+1,e}dx + \int_{x_A}^{x_I^{n+1}} \left(U^{n+1,P1} - U^{n+1,e}\right)dx. \tag{5.24}$$

https://doi.org/10.4208/cicp.190315.290316a Published online by Cambridge University Press

Evaluation of the last term of (5.24) using Lemma 5.2 gives

$$\int_{x_A}^{x_I^{n+1}} U^{n+1,P1}dx=\int_{x_A}^{x_I^{n+1}} U^{n+1,e}dx+\Delta t\cdot\mathcal{O}(p_I^e-p_L)^3. \tag{5.25}$$

On the other hand, since

$$F_{IL}^{P1}-u_I^{P1}U_{IL}^{P1}=\left[0,p_I^{P1},u_I^{P1}p_I^{P1}\right]^T, \tag{5.26}$$

we can easily get

$$F_{IL}^{P1}-u_I^{P1}U_{IL}^{P1}=F_{IL}^{e}-u_I^{e}U_{IL}^{e}+\mathcal{O}(p_I^e-p_L)^3, \tag{5.27}$$

using Lemma 5.2 once again. Substitution of (5.25) and (5.27) into (5.21) leads to error estimate (1). Likewise, the conservation error (2) is also held for the medium on the right-hand side of the interface. The sum of error estimate (2) and (3) leads to the total conservation error (3). □

According to Lemma 5.2 and 5.3, we have the following conclusion on the interface accuracy and local conservation error for the PGFM.

Theorem 5.2. *When applied to treat the interface for the multi-medium Riemann problem* (2.1)*, the PGFM has the interface error and the local conservation error of both "third-order accuracy" with an error estimate of* $\mathcal{O}(p_I^e-p_L)^3$ *or* $\mathcal{O}(p_I^e-p_R)^3$ *regardless of the solution type.*

6 Discussion on the error in GFMs

The above sections support a conclusion that an appropriate definition of the ghost fluid state would not have any impact on the real fluid. However, overheating errors are usually localized close to the interface, even with appropriate definitions of the ghost fluid state. In this section, we further investigate the error generation and suppression by different numerical treatments for multi-medium Riemann problems.

6.1 Error generation for treating multi-medium Riemann problem

Here we use the same initial conditions of gas-water Riemann problem (4.15) to study the main source of error. The numerical solutions, compared with the exact solution, are obtained by three numerical treatments: (1) multi-medium Riemann solver for multi-medium flow; (2) single-medium Riemann solver for single-medium flow; (3) multi-medium Riemann solver for single-medium flow. Without loss of generality, the ghost fluid state is defined via using Approach A (basic idea of the MGFM) or Approach B (basic idea of the PGFM) in Section 5.2. That is to say, the ghost fluid region consists of no Riemann wave or a mirrored wave structure as in the real fluid.

https://doi.org/10.4208/cicp.190315.290316a Published online by Cambridge University Press

(1) **Multi-medium Riemann solver for multi-medium flow:** For a multi-medium Riemann solver, we should define two GFM Riemann problems in each time step. The treatment adopted here is to define the ghost fluid state exactly. For example, the parameters and initial conditions of GFM Riemann problems (3.11) and (3.12) for the first step of computation are respectively listed in Tables 3 and 4. These GFM Riemann problems are then solved by the second-order MUSCL-based HLL approximate Riemann solver [34], respectively. Finally, the solution over whole computation domain is obtained according to the new interface location, and then the next time step is proceeded.

Table 3: Parameters and initial conditions of GFM Riemann problem (3.11) at the first time step.

Approach	γ_L	B_L	p_L	ρ_L	u_L	γ_R^*	B_R^*	p_R^*	ρ_R^*	u_R^*
A	1.4	0.0	8000.0	0.7	-80.0	1.4	0.0	2593.362	0.313	14.012
B	1.4	0.0	8000.0	0.7	-80.0	1.4	0.0	8000.0	0.7	108.023

Table 4: Parameters and initial conditions of GFM Riemann problem (3.12) at the first time step.

Approach	γ_L^*	B_L^*	p_L^*	ρ_L^*	u_L^*	γ_R	B_R	p_R	ρ_R	u_R
A	7.15	3309.0	2593.362	1.082	14.012	7.15	3309.0	1.0	1.0	0.0
B	7.15	3309.0	1.0	1.0	28.023	7.15	3309.0	1.0	1.0	0.0

(2) **Single-medium Riemann solver for single-medium flow:** To compare with the exact solution, we design two single-medium Riemann problems with only one-sided fluid state deserving special attention. In each Riemann problem, one-sided initial fluid state should be purpose-designed to make the flow state on the other side be consistent with the state of the original multi-medium Riemann problem. These two Riemann problems are called consistent Riemann problems in this paper and respectively written as

$$\frac{\partial U}{\partial t}+\frac{\partial F(U)}{\partial x}=0, \quad U|_{t=0}=\begin{cases} U_L, & x<x_0, \\ \widetilde{U_R}, & x>x_0. \end{cases} \tag{6.1}$$

and

$$\frac{\partial U}{\partial t}+\frac{\partial F(U)}{\partial x}=0, \quad U|_{t=0}=\begin{cases} \widetilde{U_L}, & x<x_0, \\ U_R, & x>x_0. \end{cases} \tag{6.2}$$

Hereafter, "$\sim$" indicates the purpose-designed fluid (state). The state $\widetilde{U_L}$ or $\widetilde{U_R}$ is defined as the similar way in Table 2, where the interfacial states are solved exactly. Tables 5 and 6 shows parameters and initial conditions for different approaches and media. The initial data are the same as that in Tables 3 and 4. We use the second-order MUSCL-based HLL approximate Riemann solver to solve these single-medium Riemann problems.

(3) **Multi-medium Riemann solver for single-medium flow:** Two single-medium Riemann problems are obtained as in Tables 5 and 6. In this treatment, these single-medium Riemann problems are solved as two multi-medium Riemann problems.

https://doi.org/10.4208/cicp.190315.290316a Published online by Cambridge University Press

Table 5: Parameters and initial conditions of consistent Riemann problem (6.1).

Approach	γ_L	B_L	p_L	ρ_L	u_L	$\widetilde{\gamma_R}$	$\widetilde{B_R}$	$\widetilde{p_R}$	$\widetilde{\rho_R}$	$\widetilde{u_R}$
A	1.4	0.0	8000.0	0.7	-80.0	1.4	0.0	2593.362	0.313	14.012
B	1.4	0.0	8000.0	0.7	-80.0	1.4	0.0	8000.0	0.7	108.023

Table 6: Parameters and initial conditions of consistent Riemann problem (6.2).

Approach	$\widetilde{\gamma_L}$	$\widetilde{B_L}$	$\widetilde{p_L}$	$\widetilde{\rho_L}$	$\widetilde{u_L}$	γ_R	B_R	p_R	ρ_R	u_R
A	7.15	3309.0	2593.362	1.082	14.012	7.15	3309.0	1.0	1.0	0.0
B	7.15	3309.0	1.0	1.0	28.023	7.15	3309.0	1.0	1.0	0.0

Figs. 8 and 9 show the global and local density profiles at $t = 1.5\times10^{-3}$. In these figures, "MMRS-MMF" represents the Multi-Medium Riemann Solver for Multi-Medium Flow, "SMRS-SMF" represents the Single-Medium Riemann Solver for Single-Medium Flow, "MMRS-SMF" represents the Multi-Medium Riemann Solver for Single-Medium Flow. We are only interested in the computational domain where the numerical solution of Riemann problem (6.1) or (6.2) is consistent with the exact solution of original multi-medium Riemann problem. In the region of interest, there is no obvious difference among the solutions of "MMRS-MMF", "SMRS-SMF" and "MMRS-SMF", whether using Approach A or using Approach B. This further validates the correction of these definitions of the ghost fluid state. It should be noted that a large trough clearly appears near the material interface in local density profiles, which are the zoomed-in view of the density profile close to the interface. This overheating phenomenon of underpredicting the density is induced by the numerical scheme. Even though a completely single-medium HLL Riemann solver is used to solve the single-medium flow, the error is inevitable.

6.2 Error suppression techniques

In the gas-water Riemann problem (4.15), the density errors at the material interface, as shown above, are induced by the single-medium numerical scheme in essence, instead of the GFM itself. In the following, we want to equip the PGFM with some correction procedures to suppress this unphysical phenomenon.

Since the entropy advects with material velocity, there is no entropy exchange between the two fluids. This allows the entropy to be extended to the ghost fluid region [15], which can then be used to compute the density for the ghost fluid. This isentropic fix works very well for the MGFM [17]. Similarly, we can employ the similar way to redefine the density of the ghost fluid in the PGFM. The definition for pressure and density of the ghost fluid by the PGFM leads to the same entropy as in the real fluid. However, the error induced by the single-medium numerical scheme results in the change of entropy. In the PGFM, the reference entropy of "good point" in the real fluid region can be utilized to correct the entropy of "bad points"in numerical simulations. In order to overcome the

https://doi.org/10.4208/cicp.190315.290316a Published online by Cambridge University Press

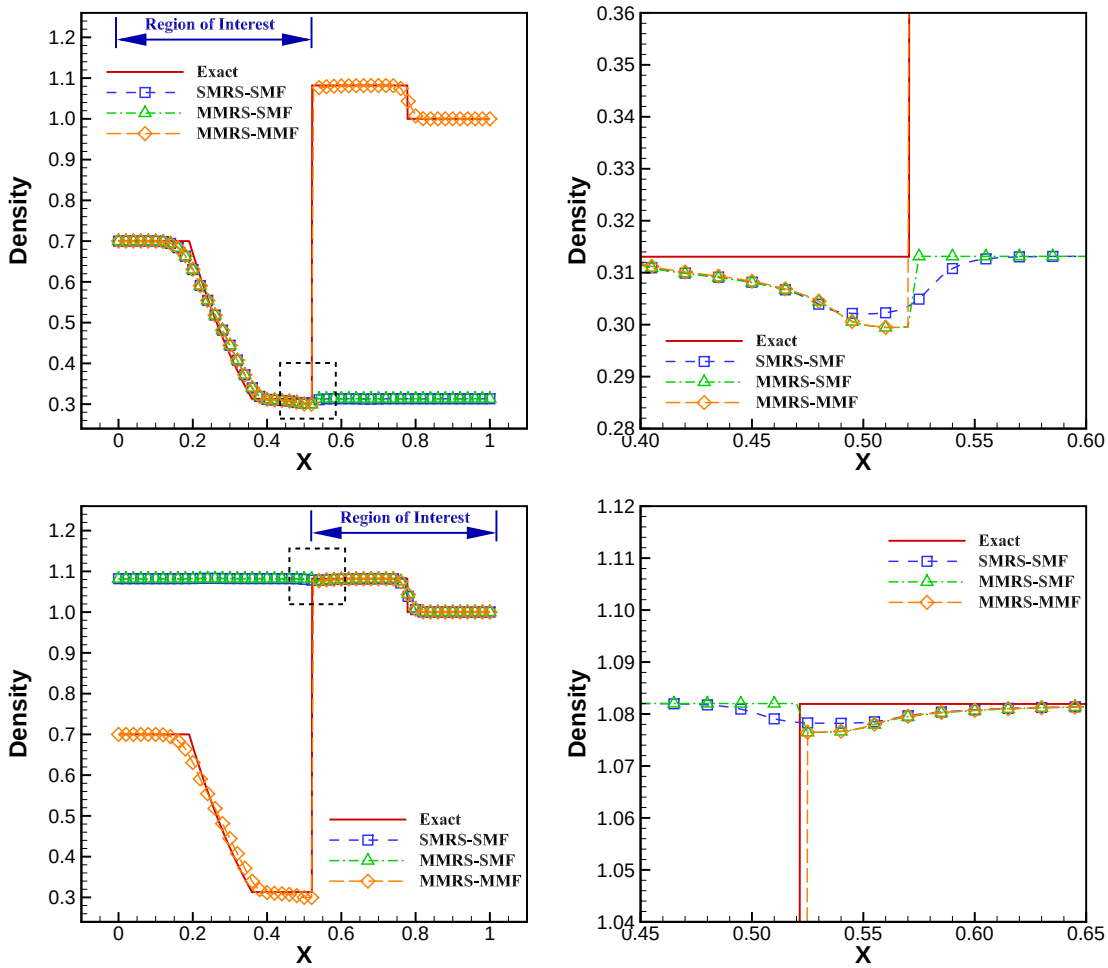


Figure 8: Density profiles obtained by Approach A. Top: Air medium on the left side; Bottom: Water medium on the right side. Left: Global profile; Right: Local profile.

influence of the single-medium numerical scheme, these "bad points" include the points near the interface, whether in the real fluid region or in the ghost fluid region. The density of these "bad points" can be modified according to the isentropic relationship

$$e(p_j,v_j)-e(p_0,v_0)=-\int_{v_0}^{v_j} p\mathrm{d}v, \tag{6.3}$$

where the subscript "0" represents the reference point (good point) and the subscript "j" represents the points needed to implement the density correction (bad points). It should be pointed out that the reference entropy in the MGFM is from the interface (as s_{IL} in Fig. 3) and obtained by the step of predicting the interfacial state. Because the state in ghost fluid region is identified with the interfacial state, the entropy of these points is also equivalent to the interfacial entropy.

https://doi.org/10.4208/cicp.190315.290316a Published online by Cambridge University Press

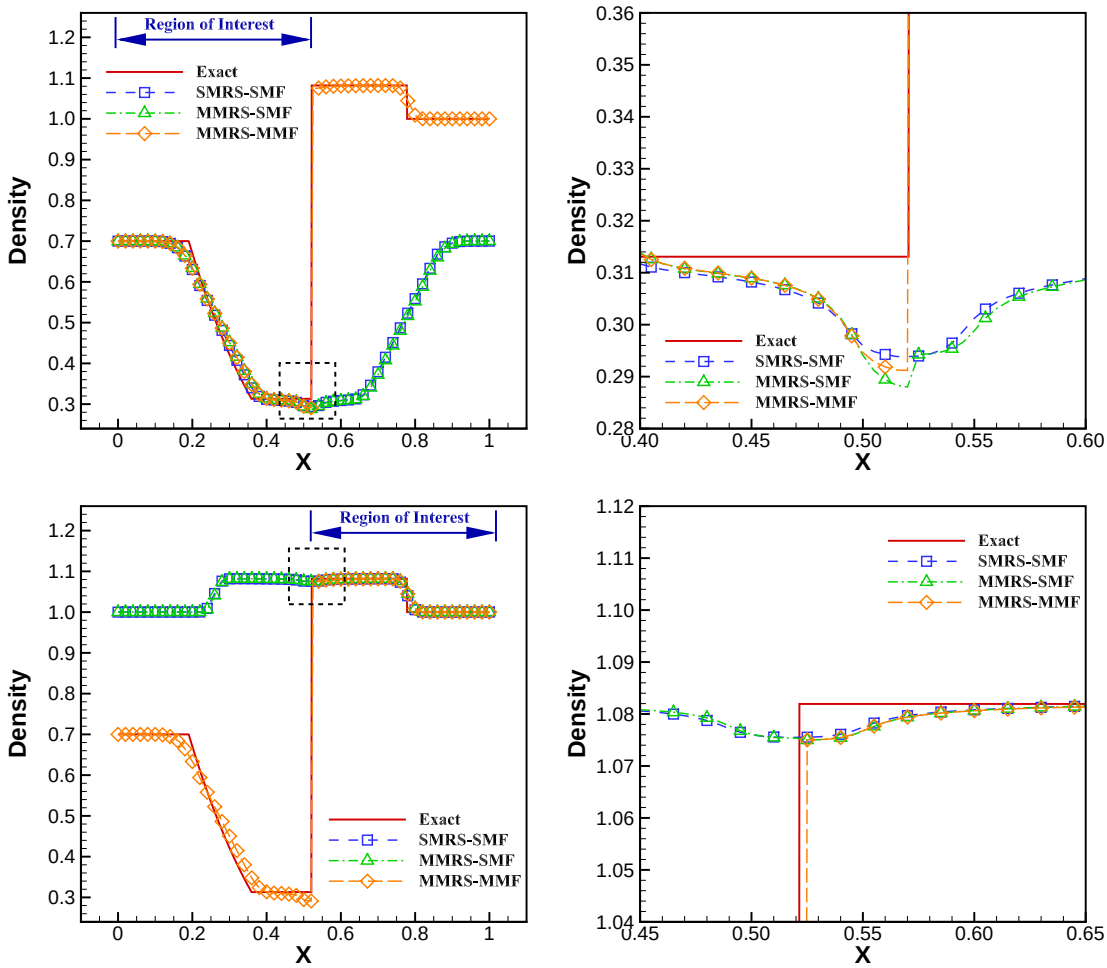


Figure 9: Density profiles obtained by Approach B. Top: Air medium on the left side; Bottom: Water medium on the right side. Left: Global profile; Right: Local profile.

However, if a moving shock is near the interface, the entropy is discontinuous essentially. Especially at the moment of a strong shock impacting on a material interface, the isentropic fix may be insufficient to fully suppress the unphysical phenomenon. In this situation, we can fix the density of "bad points" by utilizing the shock relationship, which can be written as

$$e(p_j,v_j)-e(p_0,v_0)=\frac{1}{2}(p_j+p_0)\,(v_0-v_j)\,. \tag{6.4}$$

Expression (5.15) mentions a fact that the modified density by the isentropic relationship (6.3) is "third-order" approximation to that by the shock relationship (6.4). This implies that weak shock waves are nearly isentropic. The combination of (6.3) and (6.4)

https://doi.org/10.4208/cicp.190315.290316a Published online by Cambridge University Press

gives another more acceptable choice

$$e(p_j,v_j)-e(p_0,v_0)=\begin{cases}-\int_{v_0}^{v_j} p\mathrm{d}v, & \text{if } p_j\le p_0,\\ \frac{1}{2}(p_j+p_0)(v_0-v_j), & \text{if } p_j>p_0,\end{cases} \tag{6.5}$$

which means these two basic density-correction techniques can be selected automatically. In order to distinguish clearly, the PGFM with density-correction technique (6.3), (6.4) and (6.5) are respectively called the PGFM+1, the PGFM+2 and the PGFM+A.

Note that up to this point no assumption on the general EOS (2.3) has been made. By using (2.4) into (6.3)-(6.5) and performing some algebraic manipulations, we can derive these density-correction technique with EOS (2.4). For Medium 1, the modified density in the PGFM+1, PGFM+2 and PGFM+A can be respectively written as

$$\rho_j=\rho_0\left(\frac{\overline{p}_j}{\overline{p}_0}\right)^{\frac{1}{\gamma_L}}, \tag{6.6}$$

$$\rho_j=\rho_0\left[\frac{(\gamma_L-1)\overline{p}_0+(\gamma_L+1)\overline{p}_j}{(\gamma_L-1)\overline{p}_j+(\gamma_L+1)\overline{p}_0}\right], \tag{6.7}$$

and

$$\rho_j=\begin{cases}\rho_0\left(\frac{\overline{p}_j}{\overline{p}_0}\right)^{\frac{1}{\gamma_L}}, & \text{if } p_j\le p_0,\\ \rho_0\left[\frac{(\gamma_L-1)\overline{p}_0+(\gamma_L+1)\overline{p}_j}{(\gamma_L-1)\overline{p}_j+(\gamma_L+1)\overline{p}_0}\right], & \text{if } p_j>p_0.\end{cases} \tag{6.8}$$

The above demonstration of PGFM with density-correction technique can be seen in Fig. 10. The density for Medium 2 can be defined in a similar way.

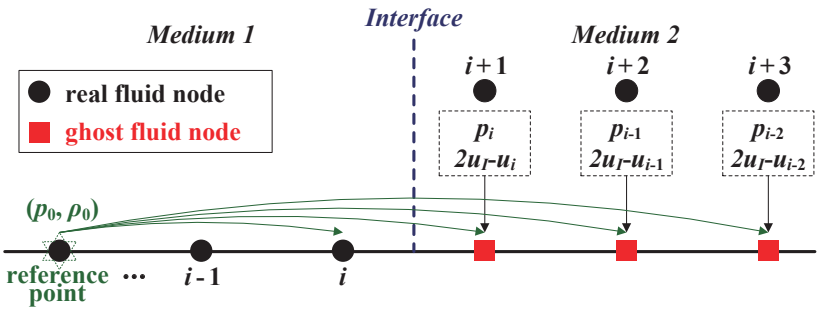


Figure 10: Illustration of the PGFM with density-correction technique for defining the ghost fluid state of Medium 1.

https://doi.org/10.4208/cicp.190315.290316a Published online by Cambridge University Press

7 Validation and numerical experiment

In this section, several one- and two-dimensional numerical examples are presented to show the performance of PGFM. The second-order MUSCL-based HLL approximate Riemann solver is used as the single-medium solver.

7.1 One-dimensional example

In the following, a test is designed to validate the conclusion in Theorem 5.2 from the numerical viewpoint. In addition, several one-dimensional examples are given to demonstrate the capability of PGFM with or without the above density-correction techniques. All the parameters are chosen to nondimensionalize the governing equations.

Case 1: Validation of the accuracy of the PGFM. We construct and solve a set of air-water Riemann problems to validate the accuracy analysis of the PGFM. The right initial states are fixed by $\rho_R = 1.0$, $u_R = 0.0$, $p_R = 100.0$. The left density and velocity are also fixed by $\rho_L = 1.0$, $u_L = 0.0$. The left pressure p_L can be selected to make $p_I^e/p_R - 1$ halved repeatedly. The nonlinear wave in the right side can be a shock wave if $p_I^e/p_R - 1 > 0$, or a rarefaction wave if $p_I^e/p_R - 1 < 0$. For the test on conservation error, the computation domain $[x_A, x_B]$ is [0, 1] and the initial interface location is chosen as 0.5. The exact results are obtained at time $t = 1.0 \times 10^{-3}$. In order to obtain accurate results to the full extent, we get the exact solutions of relative GFM Riemann problems without any influence of numerical schemes. This test method is similar to that in [30]. Tables 7 and 8 respectively list the orders of interface accuracy and conservation error by the PGFM. The results show that the PGFM indeed has "third-order" interface accuracy and local conservation error. Specially, for the conservation error test where a rarefaction wave is generated, machine error is unavoidable due to the evaluation of the first integral in (5.22) with a numerical integration algorithm. When the interface is near in balance, the proportion of machine error to conservation error is large enough to affect the accuracy test. The results in this case, therefore, are only shown down to $p_I^e/p_R - 1 = -0.1$ in Table 8.

Case 2: Strong shock impacting on a gas-gas interface. In this case, an incident shock from the left gas medium is transmitted into another gas medium and there should be no wave reflection. This is similar to the shock impedance matching problems as discussed in [17]. The parameters and initial conditions are identical to Problem 6 in [17] and given in (7.1).

$$\begin{cases} x < 0.2: & (\gamma_L, B_L, \rho_L, u_L, p_L) = (1.667, 0.0, 3.175962, 9.434992, 100.0), \\ x > 0.2: & (\gamma_R, B_R, \rho_R, u_R, p_R) = (1.2, 0.0, 1.0, 0.0, 1.0). \end{cases} \tag{7.1}$$

Such critical conditions are very difficult to maintain and enforce by any GFM algorithm due to its manner of obtaining solution via computation in the single-medium flow. 201 uniform mesh points are distributed in domain [0, 1]. The numerical solutions (symbols) at time $t = 0.045$ are drawn every fourth data point in Fig. 11. The dashed circle represents

https://doi.org/10.4208/cicp.190315.290316a Published online by Cambridge University Press

Table 7: The order of right-medium interface accuracy by the PGFM.

p_I^e/p_R-1	$\lvert p_I^{P2}-p_I^e\rvert$	Order	$\lvert u_I^{P2}-u_I^e\rvert$	Order	$\lvert \rho_{IR}^{P2}-\rho_{IR}^e\rvert$	Order
0.5	3.868E-05	–	2.457E-07	–	1.567E-09	–
0.25	5.516E-06	2.81	3.514E-08	2.81	2.249E-10	2.80
0.125	7.422E-07	2.89	4.744E-09	2.89	3.036E-11	2.89
0.0625	9.659E-08	2.94	6.180E-10	2.94	3.960E-12	2.94
0.03125	1.233E-08	2.97	7.894E-11	2.97	5.000E-13	2.99
0.015625	1.558E-09	2.98	9.976E-12	2.98	6.994E-14	2.84
-0.5	2.819E-04	–	1.821E-06	–	1.171E-08	–
-0.25	3.465E-05	3.02	2.229E-07	3.03	1.431E-09	3.03
-0.125	4.299E-06	3.01	2.759E-08	3.01	1.769E-10	3.02
-0.0625	5.354E-07	3.01	3.433E-09	3.01	2.200E-11	3.01
-0.03125	6.680E-08	3.00	4.281E-10	3.00	2.743E-12	3.00
-0.015625	8.342E-09	3.00	5.345E-11	3.00	3.431E-13	3.00

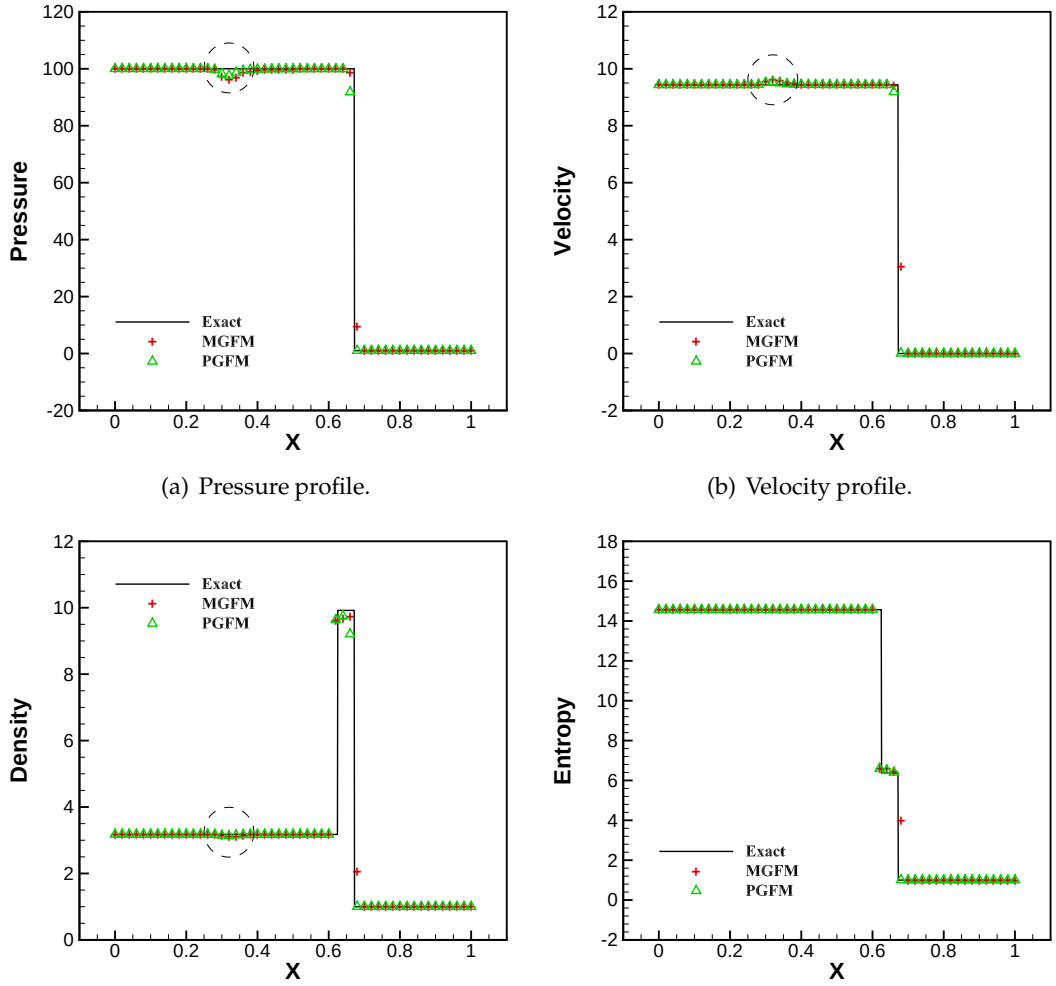
Table 8: The order of right-medium conservation error by the PGFM.

p_I^e/p_R-1	Mass	Order	Momentum	Order	Energy	Order
0.5	2.462E-07	–	7.853E-08	–	9.513E-04	–
0.25	3.518E-08	2.81	5.622E-09	3.80	1.359E-04	2.81
0.125	4.746E-09	2.89	3.796E-10	3.89	1.834E-05	2.89
0.0625	6.182E-10	2.94	2.473E-11	3.94	2.388E-06	2.94
0.03125	7.894E-11	2.97	1.582E-12	3.97	3.050E-07	2.97
0.015625	9.992E-12	2.98	1.026E-13	3.95	3.871E-08	2.98
-0.8	7.668E-06	–	-3.951E-06	–	2.963E-02	–
-0.4	9.186E-07	3.06	-2.362E-07	4.06	3.585E-03	3.05
-0.2	1.151E-07	3.00	-1.389E-08	4.09	4.642E-04	2.95
-0.1	8.675E-09	3.73	-1.165E-09	3.57	8.136E-05	2.51

the location of the unphysical reflection phenomenon. Figs. 11(a)-11(c) show that both the MGFM and the PGFM are not completely able to remove the unphysical reflection in the pressure, velocity and density profiles for this case. Fig. 11(d) shows that there is no presence of unphysical reflection in the entropy profile. Note that the performance of these two numerical methods is almost the same. This is because the definition of the ghost fluid state for the left medium results in the same solution type $W\dot{:}-^*$ for both MGFM and PGFM.

Case 3: Performance of the MGFM and the PGFM. In this case, we show the performance of MGFM and PGFM by solving the same multi-medium Riemann problem (4.15). 201 uniform mesh points are distributed in domain [0, 1]. The pressure, velocity, density and entropy plots are respectively displayed in Fig. 12. The insert shows the

https://doi.org/10.4208/cicp.190315.290316a Published online by Cambridge University Press



(a) Pressure profile.

(b) Velocity profile.

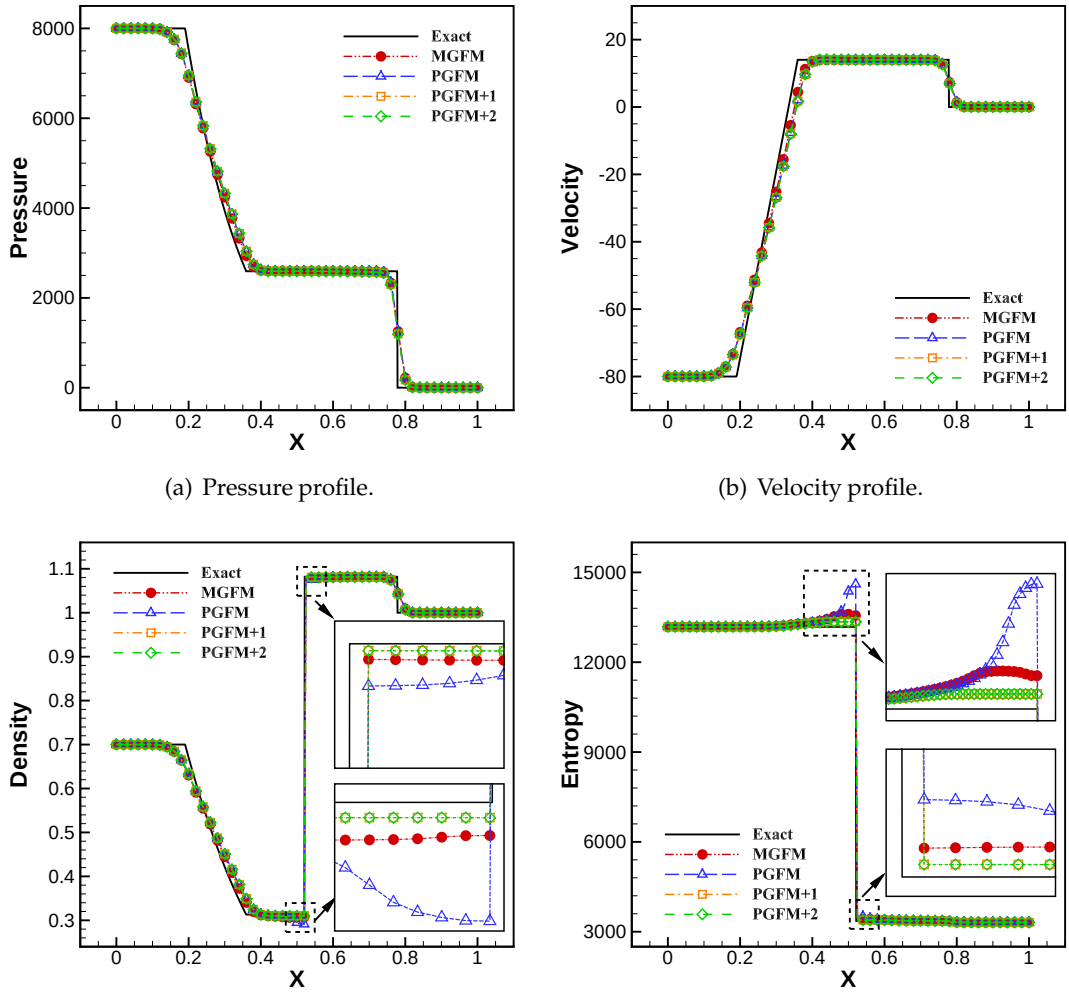
(c) Density profile.

(d) Entropy profile.

Figure 11: Performance of numerical methods for the shock impedance matching problem.

zoomed-in view of the density or entropy profile close to the interface. For the pressure and velocity solutions, it is obvious that the performance of these methods is very similar. However, for the density and entropy solutions, the results obtained by the methods with density-correction technique (MGFM, PGFM+1 and PGFM+2) are better than that without density-correction technique (PGFM). More specifically, in the density profile, PGFM underpredicts the density near the material interface severely. Comparatively speaking, PGFM+1 and PGFM+2 are the most accurate and nearly provide the same results. In the entropy profile, it is more evident that the PGFM produces the worst results due to the influence of numerical scheme. PGFM+1 and PGFM+2, as expected, greatly suppress this unphysical phenomenon and appear to give better results than the MGFM.

https://doi.org/10.4208/cicp.190315.290316a Published online by Cambridge University Press



(a) Pressure profile.

(b) Velocity profile.

(c) Density profile.

(d) Entropy profile.

Figure 12: Comparison of solutions by the MGFM and the PGFM.

Case 4: Performance of different density-correction techniques. This is a typical case to test the PGFM with different density-correction techniques. The water is filled stationarily inside the computational domain $[0, x_0]$ initially. Then, the right boundary, such as a piston, is moving into or out of the water with constant velocity u_b. Thus, a shock wave or a rarefaction wave is generated from the moving piston. Such prescribed boundary speed implies that the PGFM in this case is identical to the application of a reflective boundary condition. The MGFM in this case requires that the pressure p_b and density ρ_b at the right boundary should be firstly predicted, and then these predicted quantities and u_b would serve as the ghost fluid state for the computation of whole do-

https://doi.org/10.4208/cicp.190315.290316a Published online by Cambridge University Press

Table 9: Data for two moving boundary problems.

Problem	p_0	ρ_0	u_0	u_b	x_0
1	1.0	1.0	0.0	-39.3978	0.8
2	10000.0	1.0	0.0	45.1765	0.7

main. The parameters and initial conditions of two moving boundary problems are given in Table 9. The value of boundary velocity u_b is designed to make $p_b^e/p_0=10^4$ in problem 1 with the presence of a strong shock wave, or $p_0/p_b^e=10^4$ in problem 2 with the presence of a strong rarefaction wave. A total of 401 uniform mesh points are distributed in domain [0, 1]. Excessive fluid cells beyond the ghost fluid region are reserved to allow moving of the boundary. In order to highlight the features of different density-correction techniques, the reference point is specially chosen as the left end point.

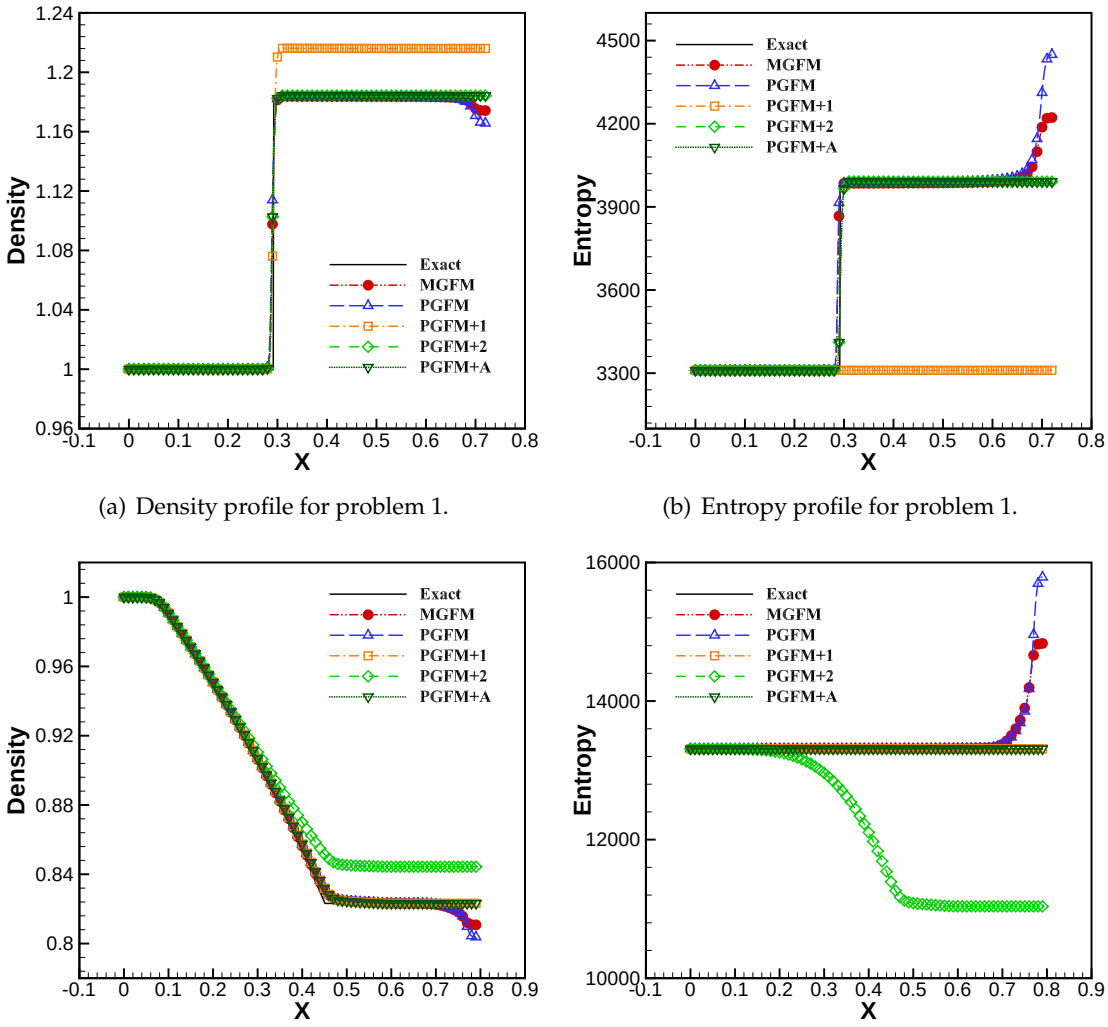
As shown in Case 3, there is little distinction between different methods in the pressure or velocity profile. Therefore, we are only concerned with the results of density and entropy. The numerical solutions at time $t=2.0\times10^{-3}$ for both problems are shown in Fig. 13. Generally speaking, the MGFM provides better results than the PGFM. But the overheating phenomenon at the right boundary is also obvious enough for the MGFM in this specific case. Although the density near the interface is modified in the MGFM, the correction is not so powerful to fully suppress the unphysical solutions. If the PGFM+1 is used in problem 1, there are large density error found behind the shock in Fig. 13(a) and unphysical entropy in Fig. 13(b). The PGFM+2, derived from the shock relationship, produces satisfying solutions. On the contrary, if the PGFM+2 is used in problem 2, there is distinctly visible error in Figs. 13(c) and 13(d). The results obtained by the PGFM+1, as expected, concur well with the exact solution. Nevertheless, the PGFM+A behaves well in any problem.

Several curves in Fig. 14 record the error history (i.e. $|w_b(t)-w_b^e(t)|/|w_b^e(t)|$) of density or entropy at the right boundary, where $w_b(t)$ and $w_b^e(t)$ are the numerical solution and the exact solution, respectively. It is clear that large oscillations of density error are produced for all the methods during the early time period. Then, the errors have no significant change as time progresses. Comparatively speaking, PGFM+A are more accurate than MGFM and PGFM. PGFM+1 or PGFM+2, however, only behaves well in either problem. In Figs. 14(a) and 14(b), the performance of PGFM+2 is similar to the PGFM+A. In Figs. 14(c) and 14(d), the performance of PGFM+1 is similar to the PGFM+A. This also strongly implies that the errors of density and entropy are suppressed very well by the PGFM+A in any problem.

7.2 Two-dimensional example

In the following, several two-dimensional examples are illustrated to compare the PGFM and the MGFM. Both are equipped with the same density-correction technique (6.3) in these cases. Due to symmetry of these typical problems, only half of the computational

https://doi.org/10.4208/cicp.190315.290316a Published online by Cambridge University Press



(a) Density profile for problem 1.

(b) Entropy profile for problem 1.

(c) Density profile for problem 2.

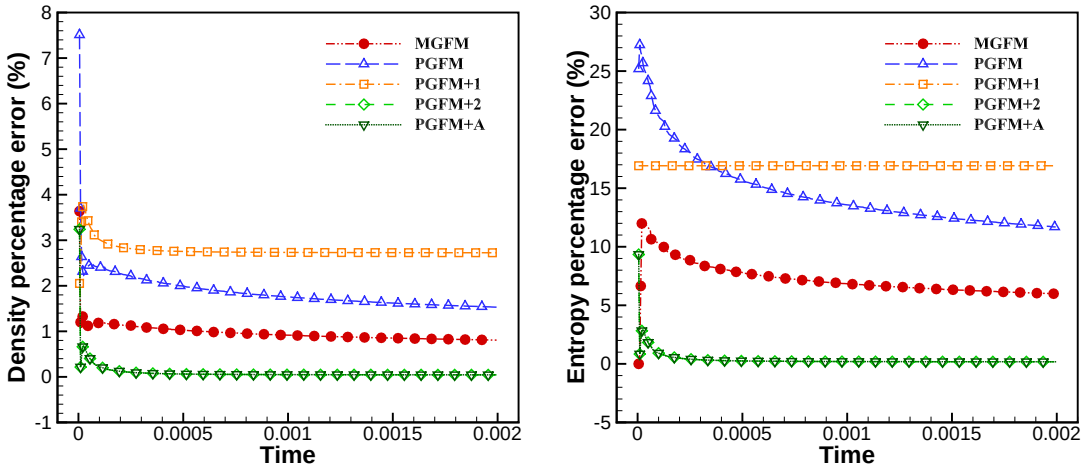
(d) Entropy profile for problem 2.

Figure 13: Comparison of solutions by the MGFM and the PGFM with different density-correction techniques.

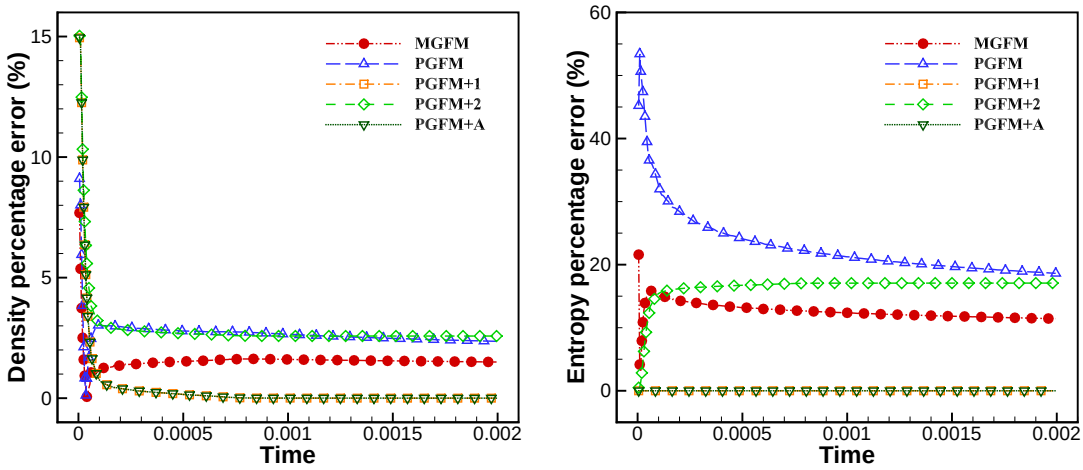
domain is plotted for comparison. To capture the moving multi-medium interface, the level set technique is utilized. All the parameters are chosen to nondimensionalize the governing equations unless otherwise noted.

Case 1: Air shock interacting with helium bubble. The example considered here corresponds to the interaction of a Mach 1.22 shock with a cylindrical helium bubble in air. This was studied both experimentally and numerically in [18, 35–37]. The initial problem configuration is given in Fig. 15. Parameters and initial conditions for air and helium are shown in Table 10. A total of 651×179 uniform grid points are distributed

https://doi.org/10.4208/cicp.190315.290316a Published online by Cambridge University Press



(a) Density error for problem 1. (b) Entropy error for problem 1.



(c) Density error for problem 2. (d) Entropy error for problem 2.

Figure 14: Comparison of percentage errors by the MGFM and the PGFM with different density-correction techniques.

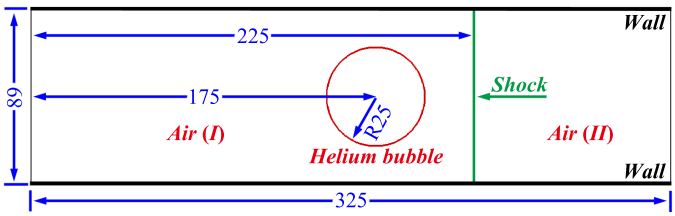


Figure 15: Geometry used for an air shock impinging on a helium bubble.

https://doi.org/10.4208/cicp.190315.290316a Published online by Cambridge University Press

Table 10: Parameters and Initial conditions for an air shock impinging on a helium bubble.

Medium	γ	B	u	v	ρ	p
Helium bubble	1.667	0.0	0.0	0.0	0.138	1.0
Air(I)	1.4	0.0	0.0	0.0	1.0	1.0
Air(II)	1.4	0.0	-0.394	0.0	1.3764	1.5698

in the computational domain. The reflective boundary conditions are used at the top and bottom, and the nonreflective boundary conditions are used at the left and right boundaries.

The experimental images [35] and numerical schlieren images obtained by the MGFM and the PGFM at different times are presented in Fig. 16. The dashed circle represents the initial bubble. When the incident shock hits the material interface, a refracted shock is created inside the bubble and an expansion wave is created upstream. As the sound speed in helium is faster than in the surrounding air, the refracted shock moves faster than the incident shock and a side shock is then created to compensate for this misalignment. The impinging shock also results in the deformation and movement of the bubble. In this figure, the multiple waves inside and outside the helium bubble are clearly visible. Both the computational results agree well with the experiments. This means these definitions of ghost fluid states are both reasonable and effective.

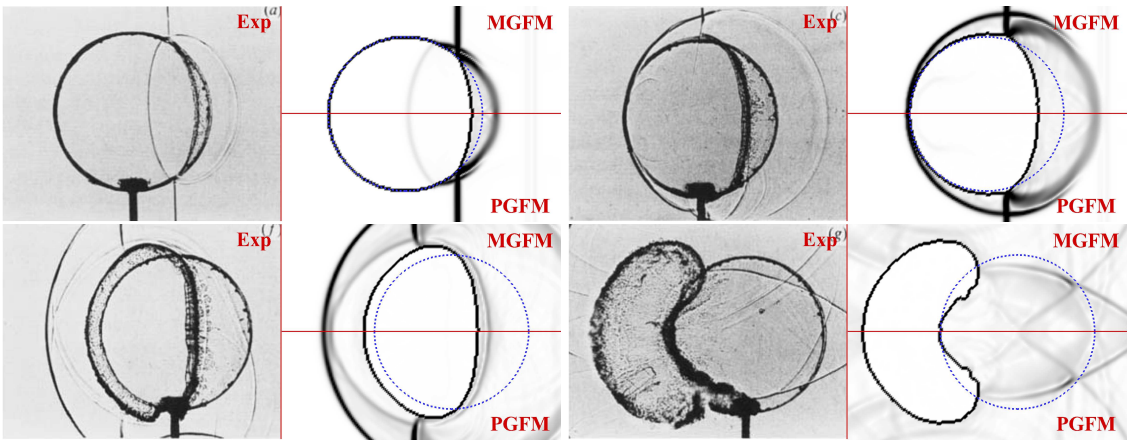


Figure 16: Comparison of experimental images and numerical schlieren images for an air shock impinging on a helium bubble.

Case 2: Water shock interacting with air bubble. Here a more challenging case is presented with greater material differences and very large pressure jumps. A cylindrical air bubble in water is impacted by a shock. The initial problem configuration is given in Fig. 17. Parameters and initial conditions for water and air are shown in Table 11. This problem is similar to that proposed in [18]. A total of 601×601 uniform grid points

https://doi.org/10.4208/cicp.190315.290316a Published online by Cambridge University Press

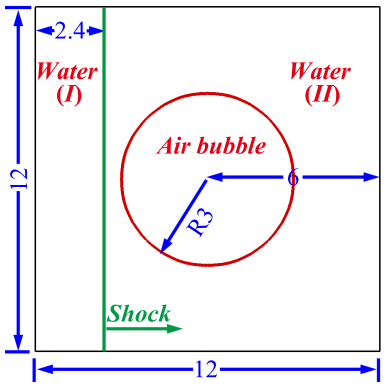


Figure 17: Geometry used for a water shock impinging on an air bubble.

Table 11: Parameters and Initial conditions for a water shock impinging on an air bubble.

Medium	γ	B	u	v	ρ	p
Air bubble	1.4	0.0	0.0	0.0	0.0012	1.0
Water(I)	7.15	3309.0	67.32	0.0	1.31	19000.0
Water(II)	7.15	3309.0	0.0	0.0	1.0	1.0

are distributed in the computational domain. The nonreflective boundary conditions are used for all the fluid outside boundaries.

The numerical density contours obtained by the MGFM and the PGFM at different times are presented in Fig. 18. The dynamic process of bubble including deformation and collapse is clearly shown in this figure. Compared to the initial bubble, the impinging shock deforms the front portion of the air bubble, leaving the leeward side unaffected for a long time. At last, a very high speed jet is formed at the leeward side. Meanwhile, the pressure and the density increase due to a "water-hammer" effect. The serial results by the PGFM are in good agreement with that by the MGFM.

Case 3: Underwater explosion near a free surface. In the following calculations, we assume that a cylindrical explosive source beneath a free surface (gas-water interface). The free surface is initially located at the straight line $y=2.5$m. An explosive gas bubble with a radius of 1.0m is located at the origin $(0.0,0.0)$ in water. The computational domain is a rectangular region with $X\times Y\in[-5\text{m},5\text{m}]\times[-5\text{m},5\text{m}]$. Parameters and initial conditions for these three fluids are shown in Table 12. Actually, this problem is similar to that proposed in [38]. A total of 201×201 uniform grid points are distributed in the computational domain. The nonreflective boundary conditions are used for all the fluid outside boundaries.

Once the explosion starts, a strong underwater shock is generated below the free surface and propagates radially outwards with decreasing strength. After reaching the free surface, the impinging shock results in a transmitted shock wave and a reflected rarefaction wave. The reflected rarefaction wave, upon contacting the expanded bubble, further

https://doi.org/10.4208/cicp.190315.290316a Published online by Cambridge University Press

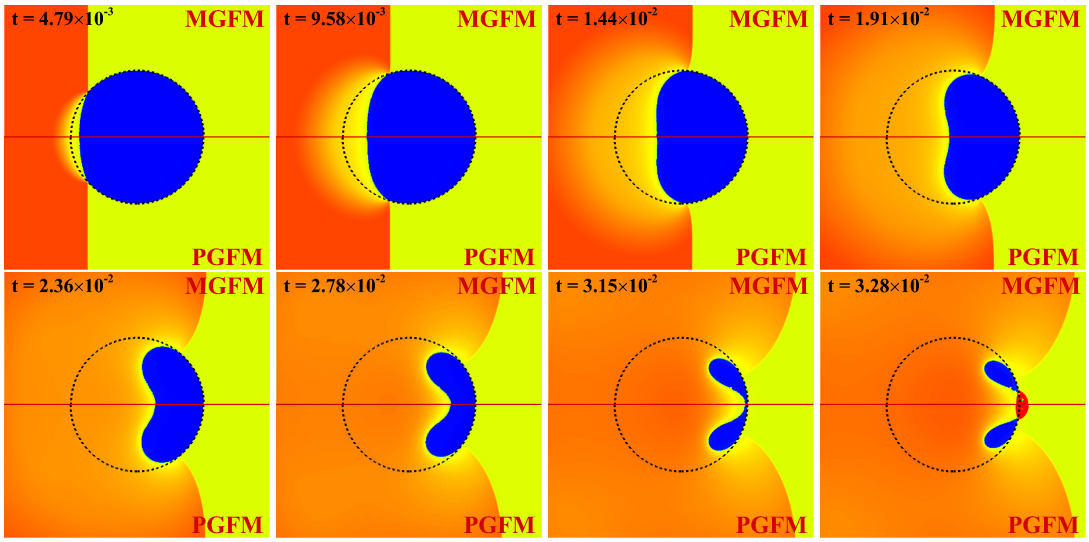


Figure 18: Comparison of density contours for a water shock impinging on an air bubble by the MGFM and the PGFM.

Table 12: Parameters and Initial conditions for underwater explosion.

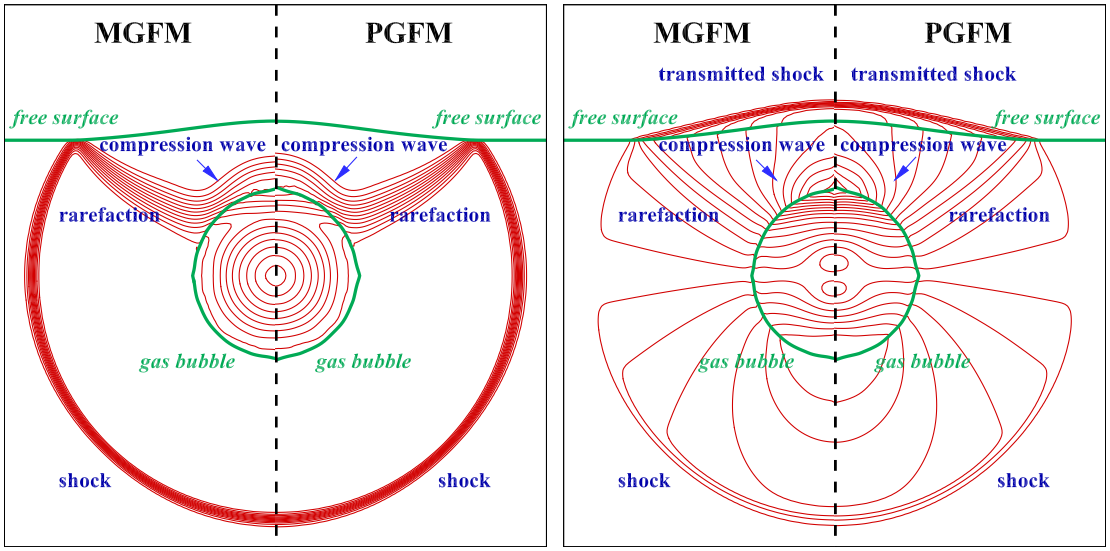
Medium	γ	B (Pa)	u (m/s)	v (m/s)	ρ (kg/m^3)	p (Pa)
Bubble	2.0	0.0	0.0	0.0	1.27×10^3	8.29×10^8
Water	7.15	3.309×10^8	0.0	0.0	1.0×10^3	1.0×10^5
Air	1.4	0.0	0.0	0.0	1.0	1.0×10^5

degenerates into a transmitted rarefaction wave and a reflected compression wave. The pressure contour and y-velocity (v) contour at $t=1.8$ms obtained by the MGFM and the PGFM are presented in Fig. 19. Numerical results are displayed symmetrically with same contours. Fig. 19(a) shows that the pressure features remain almost the same between the MGFM and the PGFM. Only imperceptible difference exists near the top of the expanded bubble. The transmitted shock wave in the air is relatively much weaker and can not be discerned in the present pressure plot with limited contour lines. Fig. 19(b) shows the contour of velocity component in the y-direction. In this figure, the shock front transmitted in the air is clearly displayed. All the main and local features of the flow are successfully captured by both methods and almost exactly the same.

8 Conclusions

The issue of reasonable definition of the ghost fluid state was studied. Conditions associated with the ghost fluid state and exact interfacial state were established and all possible treatments in GFMs were considered and evaluated. In general, there are infinitely many ways to reasonably define the ghost fluid state. But essentially only six wave patterns

https://doi.org/10.4208/cicp.190315.290316a Published online by Cambridge University Press



(a) Pressure contour. (b) Y-velocity contour.

Figure 19: Comparison of flow fields of underwater explosions by the MGFM and the PGFM at $t=1.8$ms.

can exist in the ghost fluid region. A practical GFM, followed by this methodology, was developed to resolve the interface dynamics for embedded fluid-fluid interfaces. In this method, the way to define the ghost fluid state is simple and reasonable and high-order accurate. Compared with the MGFM, this treatment only requires one interfacial quantity (velocity) contributing to defining the ghost fluid state.

However, numerical errors may appear at the material interface for some extreme cases of multi-medium compressible flows. It was found that these errors are induced by the single-medium numerical scheme in essence, instead of the GFM itself. With the help of density-correction techniques, the PGFM significantly suppressed this unphysical phenomenon at the material interface, and was found to be consistent in generating satisfactory solutions for several typical problems.

Acknowledgments

The authors would like to thank the referees for valuable comments and suggestions. This work is supported under the National Natural Science Foundation of China (No. 11201442).

References

[1] B. Larrouturou, How to preserve the mass fractions positivity when computing compressible multi-component flows, J. Comput. Phys., 95 (1991), 59-84.

https://doi.org/10.4208/cicp.190315.290316a Published online by Cambridge University Press

[2] S. Karni, Multicomponent flow calculations by a consistent primitive algorithm, J. Comput. Phys., 112 (1994), 31-43.
[3] S. Karni, Hybrid multifluid algorithms, SIAM J. Sci. Comput., 17 (1996), 1019-1039.
[4] R. Abgrall, How to prevent oscillations in multicomponent flow calculations: a quasi conservative approach, J. Comput. Phys., 125 (1996), 150-160.
[5] P. Jenny, B. Muller and H. Thomann, Correction of conservative Euler solvers for gas mixtures, J. Comput. Phys., 132 (1997), 91-107.
[6] R. Abgrall and S. Karni, Computations of compressible multifluids, J. Comput. Phys., 169 (2001), 594-623.
[7] E. H. van Brummelen and B. Koren, A pressure-invariant conservative Godunov-type method for barotropic two-fluid flows, J. Comput. Phys., 185 (2003), 289-308.
[8] R. R. Nourgaliev, T. N. Dinh and T. G. Theofanous, Adaptive characteristics-based matching for compressible multifluid dynamics, J. Comput. Phys., 213 (2006), 500-529.
[9] E. Johnsen and T. Colonius, Implementation of WENO schemes in compressible multicomponent flow problems, J. Comput. Phys., 219 (2006), 715-732.
[10] C. Hirt and B. Nichols, Volume of fluid (VOF) method for the dynamics of free boundaries, J. Comput. Phys., 39 (1981), 201-225.
[11] M. Sussman, P. Smereka and S. Osher, A level set approach for computing solutions to incompressible two-phase flow, J. Comput. Phys., 114 (1994), 146-159.
[12] S. O. Unverdi and G. Tryggvason, A front-tracking method for viscous incompressible multifluid flows, J. Comput. Phys., 100 (1992), 25-37.
[13] J. Glimm, D. Marchesin and O. McBryan, Subgrid resolution of fluid discontinuities, II, J. Comput. Phys., 37 (1980), 336-354.
[14] J. Glimm, D. Marchesin and O. McBryan, A numerical method for two phase flow with an unstable interface, J. Comput. Phys., 39 (1981), 179-200.
[15] R. P. Fedkiw, T. Aslam, B. Merriman and S. Osher, A non-oscillatory Eulerian approach to interfaces in multimaterial flows (the ghost fluid method), J. Comput. Phys., 152 (1999), 457-492.
[16] R. P. Fedkiw, Coupling an Eulerian fluid calculation to a Lagrangian solid calculation with the ghost fluid method, J. Comput. Phys., 175 (2002), 200-224.
[17] T. G. Liu, B. C. Khoo and K. S. Yeo, Ghost fluid method for strong shock impacting on material interface, J. Comput. Phys., 190 (2003), 651-681.
[18] X. Y. Hu and B. C. Khoo, An interface interaction method for compressible multifluids, J. Comput. Phys., 198 (2004), 35-64.
[19] C. W. Wang, T. G. Liu and B. C. Khoo, A real-ghost fluid method for the simulation of multimedium compressible flow, SIAM J. Sci. Comput., 28 (2006), 278-302.
[20] T. G. Liu, B. C. Khoo and C. W. Wang, The ghost fluid method for compressible gas-water simulation, J. Comput. Phys., 204 (2005), 193-221.
[21] Y. Hao and A. Prosperetti, A numerical method for three-dimensional gas-liquid flow computations, J. Comput. Phys., 196 (2004), 126-144.
[22] C. Farhat, A. Rallu and S. Shankaran, A higher-order generalized ghost fluid method for the poor for the three-dimensional two-phase flow computation of underwater implosions, J. Comput. Phys., 227 (2008), 7674-7700.
[23] H. Terashima and G. Tryggvason, A front-tracking/ghost-fluid method for fluid interfaces in compressible flows, J. Comput. Phys., 228 (2009), 4012-4037.
[24] J. X. Qiu, T. G. Liu and B. C. Khoo, Simulations of compressible two-medium flow by Runge-Kutta discontinuous Galerkin methods with the ghost fluid method, Commun. Comput.

https://doi.org/10.4208/cicp.190315.290316a Published online by Cambridge University Press

Phys., 3 (2008), 479-504.
[25] T. G. Liu, W. F. Xie and B. C. Khoo, The modified ghost fluid method for coupling of fluid and structure constituted with hydro-elasto-plastic equation of state, SIAM J. Sci. Comput., 30 (2008), 1105-1130.
[26] T. G. Liu, B. C. Khoo and W. F. Xie, The modified ghost fluid method as applied to extreme fluid-structure interaction in the presence of cavitation, Commun. Comput. Phys., 1 (2006), 898-919.
[27] S. Sambasivan and H. S. UdayKumar, Ghost fluid method for strong shock interactions. Part 1: Fluid-fluid interfaces, AIAA Journal, 47 (2009), 2907-2922.
[28] P. T. Barton and D. Drikakis, An Eulerian method for multi-component problems in non-linear elasticity with sliding interfaces, J. Comput. Phys., 229 (2010), 5518-5540.
[29] L. Xu and T. G. Liu, Optimal error estimation of the modified ghost fluid method, Commun. Comput. Phys., 8 (2010), 403-426.
[30] L. Xu and T. G. Liu, Accuracies and conservation errors of various ghost fluid methods for multi-medium Riemann problem, J. Comput. Phys., 230 (2011), 4975-4990.
[31] R. P. Fedkiw, A. Marquina and B. Merriman, An isobaric fix for the overheating problem in multimaterial compressible flows, J. Comput. Phys., 148 (1999), 545-578.
[32] E. F. Toro, Riemann Solvers and Numerical Methods for Fluid Dynamics, Springer-Verlag Berlin Heidelbert, 1999.
[33] T. G. Liu, B. C. Khoo and K. S. Yeo, The simulation of compressible multi-medium flow. Part I: A new methodology with test applications to 1D gas-gas and gas-water cases, Comput. Fluids, 30 (2001), 291-314.
[34] A. Harten, P. D. Lax and B. van Leer, On upstream differencing and Godunov-type schemes for hyperbolic conservation laws, SIAM Rev., 25 (1983), 35-61.
[35] J. F. Haas and B. Sturtevant, Interaction of weak shock waves with cylindrical and spherical inhomogeneities, J. Fluid Mech., 181 (1987), 41-76.
[36] J. J. Quirk and S. Karni, On the dynamics of a shock-bubble interaction, J. Fluid Mech., 318 (1996), 129-163.
[37] A. Marquina and P. Mulet, A flux-split algorithm applied to conservative models for multi-component compressible flows, J. Comput. Phys., 185 (2003), 120-138.
[38] T. G. Liu, B. C. Khoo and K. S. Yeo, The simulation of compressible multi-medium flow. Part II: Applications to 2D underwater shock refraction, Comput. Fluids, 30 (2001), 315-337.

https://doi.org/10.4208/cicp.190315.290316a Published online by Cambridge University Press